Chemical and Physical Mechanisms of Calcite Dissolution in Seawater

Thesis by

John David Naviaux

In Partial Fulfillment of the Requirements for
the degree of
Doctor of Philosophy in Environmental
Science and Engineering

CALIFORNIA INSTITUTE OF TECHNOLOGY
Pasadena, California

2020
Defended October 10, 2019

© 2019

John David Naviaux
ORCID: 0000-0002-0681-3163

ACKNOWLEDGEMENTS

Academia constantly drives home the power of "we." Every project is made possible by the love and support of friends and family, and improved by the hard work and feedback of peers. Although it feels cheesy to say, this thesis is no exception. First and foremost, I would like to thank Jess for his advice and mentorship over the years. When I first came to Caltech, I barely knew anything about isotopes, let alone the oceans. It a testament to Jess's infectious intellectual curiosity that, from these humble beginnings, I dedicated the next half-decade to the study of marine chemistry (using isotopes!). This project has been the most interesting and fun one of my life, and I could not have predicted that it would involve challenges ranging from unexpected biology in the lab, to water gun fights in the middle of the Pacific Ocean. I will be forever grateful for this opportunity.

Of course, with Jess came the amazing network of people with which he has surrounded himself. I was fortunate enough to overlap with Adam, whose work served as the foundation of this project. My back-and-forths with Adam were invaluable, and he was always as excited as I was when I came running to his office with each new datapoint. My frequent trips to USC to pray to the Picarro gods were made all the better by my interactions with Will, Nick, and Sijia. Their ability to make complex equipment from random lab scraps helped to push the bounds of what I thought possible. And to the rest of the Adkins group, there is no one else with whom I'd rather drink copious amounts of coffee with every Wednesday morning.

I am also lucky to have such an amazing group of friends that have served to both support and distract when the need arose. Weekendfests with Trevor helped to ground me, as did my time free associating with the GPS crew, Alistair, Dan, Kyle, and Austin. I always looked forward to talking with Hans and Leah (of Fulbright/Funbright fame) and know that, while we may be on opposite sides of the globe, we will continue to be friends forever.

My mom and dad have also been an unwavering source of love and support. They instilled an early love of science in me, and were with me as I bounced around from psychology, to

economics, to particle physics, to finally finding my home in the environmental sciences. I could not ask for more loving and caring parents.

Of course, nothing has brought as much joy to my life as the family I have gained along the way. This is the second thesis that Tima, the best pup better than the rest pup (everybody knows it, EASY), has personally overseen, and her constant demands for walks and bellyrubs were essential to its success. Lucky for me, one of the best parts about Tima is the person that lives with her, Lauren. Lauren, even though we are both strong, independent people that are totally not co-dependent, I could not imagine my life without you. You are, without a doubt, the most impressive person I have ever met, and I am so grateful that I get to spend my life with you. You are my daily inspiration and best friend, and I am so excited to continue our adventure together. I love you to the moon and back.

ABSTRACT

Calcium carbonates are among the most abundant and reactive minerals on Earth, and their dissolution/preservation in the ocean helps to regulate changes in atmospheric pCO_2. The chemistry of the oceans has varied significantly over the past several billion years, and it is changing at an unprecedented rate today in response to anthropogenic burning of fossil fuels. The excess CO_2 from human activities is acidifying the oceans and decreasing the saturation state ($\Omega = \frac{[Ca^{2+}][CO_3^{2-}]}{K'_{sp}}$) of marine carbonates, increasing their propensity to dissolve. Despite its importance, the rate of carbonate dissolution in seawater is still described by a purely empirical expression, and the physical and chemical mechanisms setting the overall kinetics remain unknown. This stands in contrast to calcite dissolution in freshwater, where fully coupled surface-solution models have been identified. The lack of mechanistic understanding in seawater limits our ability to predict how carbonate dissolution kinetics, and therefore the buffering capacity of the ocean, are affected by changes in chemistry. This thesis advances our knowledge of the physical and chemical mechanisms responsible for carbonate dissolution by making new measurements in seawater both in the lab and *in-situ*.

I first probe the activation energy of the reaction in seawater by dissolving ^{13}C-labeled $CaCO_3$ across the full range of Ω at 5, 12, 21, and 37°C. I find that a surface-based framework is required to explain the strong non-linearity of the data near equilibrium. In this framework, dissolution proceeds by the retreat of pre-existing steps for $0.9<\Omega<1$, defect-assisted etch pit formation for $0.75<\Omega<0.9$, and homogenous etch pit formation for $0<\Omega<0.75$. I provide the first seawater estimates of kinetic coefficients (β), nucleation site densities (n_s), and step edge free energies (α) for each mechanism, as well as the activation energy for detachment from steps (ϵ_{step}) and the kinetic energy barrier to etch pit initiation (ϵ_{init}).

Next, I use a custom designed *in-situ* reactor to measure calcite dissolution rates across a transect of the North Pacific. I find that the same surface mechanisms and “critical” Ωs identified in lab also govern the dissolution of calcite in the open ocean. *In-situ* dissolution rates are ~4x slower than in the lab, but I use a combination of chemical spike experiments and measurements in archived seawater to show that this discrepancy can be explained by the presence of dissolved organic carbon *in-situ*. I propose an empirical rate equation that describes all previous *in-situ* measurements of inorganic calcite dissolution rates.

Changes in the relation between dissolution rate and Ω can be explained by the activation of different surface processes, but the surface theory cannot account for much of the near-equilibrium dissolution behavior and temperature dependence. I therefore continue on in this thesis to combine the latest speciation models with dissolution measurements in artificial seawater of varying sulfate concentrations. I find that low sulfate solutions suppress dissolution rates by two orders of magnitude near equilibrium, while dissolution rates in the same solutions are enhanced far-from-equilibrium. Using these results, I fit a mechanistic model of dissolution that couples surface and solution processes. The model satisfies the principle of microscopic reversibility, provides an excellent estimate of calcite solubility product in seawater, and explains near equilibrium ($\Omega > 0.75$) dissolution rates in 0, 14, and 28 mM [SO_4^{2-}] seawater at 21°C. The model cannot explain dissolution rates for $\Omega < 0.75$ when etch pits begin opening homogenously across the surface, so I suggest areas of improvement for future models.

Previous work has demonstrated that calcite dissolution rates are enhanced in the presence of the enzyme carbonic anhydrase (CA). In the final chapter of this thesis, I evaluate the mechanism of CA rate enhancement by comparing the catalytic effects of freely dissolved CA, CA immobilized within hydrogels, and CA chemically bound onto porous silica beads. At the same time, I design and test a fluidized bed reactor and demonstrate its efficacy as a carbon capture device by attaching it directly to the Caltech cogeneration power plant smokestack. I find that dissolution rates within the reactor are only enhanced when CA is freely dissolved, strongly suggesting that the catalytic mechanism is direct proton transfer from the enzyme to the calcite surface.

PUBLISHED CONTENT AND CONTRIBUTIONS

Dong, S., Adkins, J.F., Rollins, N.E., Subhas, A. V., Naviaux, J.D., Celestian, A., Liu, X., Kemnitz, N., Byrne, R.H., Berelson, W.M., 2019. Aragonite Dissolution Kinetics and Calcite/Aragonite Ratios in Sinking and Suspended Particles in the North Pacific. Earth Planet. Sci. Lett. https://doi.org/10.1016/j.epsl.2019.03.016

J.D.N. assisted with the design and testing of the equipment used to collect data. J.D.N. also organized, cleaned, and assisted with the analysis of the data.

Dong, S., Subhas, A. V., Rollins, N.E., Naviaux, J.D., Adkins, J.F., Berelson, W.M., 2018. A kinetic pressure effect on calcite dissolution in seawater. Geochim. Cosmochim. Acta 238, 411–423. https://doi.org/10.1016/j.gca.2018.07.015

J.D.N. helped to interpret the observed kinetic pressure effect by applying a model of surface energetics to the data.

Naviaux, J.D., Subhas, A. V., Dong, S., Rollins, N.E., Liu, X., Byrne, R.H., Berelson, W.M., Adkins, J.F., 2019a. Calcite dissolution rates in seawater: Lab vs. in-situ measurements and inhibition by organic matter. Mar. Chem. 215, 103684. https://doi.org/10.1016/j.marchem.2019.103684

J.D.N conducted the experiments, analyzed all of the data, and wrote the manuscript for this publication.

Naviaux, J.D., Subhas, A. V., Rollins, N.E., Dong, S., Berelson, W.M., Adkins, J.F., 2019b. Temperature Dependence of Calcite Dissolution Kinetics in Seawater. Geochim. Cosmochim. Acta 246, 363–384. https://doi.org/10.1016/J.GCA.2018.11.037

J.D.N conducted the experiments, analyzed all of the data, and wrote the manuscript for this publication.

Subhas, A. V, Adkins, J.F., Rollins, N.E., Naviaux, J., Erez, J., Berelson, W.M., 2017. Catalysis and chemical mechanisms of calcite dissolution in seawater. Proc. Natl. Acad. Sci. 114, 8175–8180. https://doi.org/10.1073/pnas.1703604114

J.D.N. assisted with the model code and helped to understand the experimental data within a surface energetic framework.

TABLE OF CONTENTS

Acknowledgements iii
Abstract v
Published Content and Contributions vii
Table of Contents viii
List of Illustrations x
List of Tables xvii
Chapter 1: Temperature Dependence of Calcite Dissolution Kinetics in Seawater. 1
  1.1 Introduction 1
  1.2 Methods 4
  1.3 Results 8
  1.4 Discussion 10
    1.1.1 Analysis within the 1-Ω framework 10
    1.4.1 Identification of changes in dissolution mechanism 16
    1.4.2 Using temperature dependence to extract physical and energetic parameters of calcite dissolution in seawater 23
    1.4.3 Role of Solution Chemistry 35
  1.5 Conclusions 36
Chapter 2: Calcite Dissolution Rates in Seawater: Lab vs. In-situ Measurements and Inhibition by Organic Matter 38
  2.1 Introduction 38
  2.2 Methods 42
    2.2.1 Description of Materials 42
    2.2.2 Laboratory Measurements of Dissolution 43
    2.2.3 *In-situ* Reactor Design and Lab Verification 45
    2.2.4 Deployment of Reactors in the Field 49
    2.2.5 Field Sampling Methods 50
    2.2.6 Quality Checking Reactors 51
  2.3 Results 52
    2.3.1 Discrepancy in Ω Calculations 52
    2.3.2 *In-situ* Dissolution Results 55
    2.3.3 Laboratory Results 58
  2.4 Discussion 61
    2.4.1 Implications for Ocean Saturation State 61
    2.4.2 Laboratory versus *In-situ* Dissolution Rates 62
    2.4.3 Role of Inhibitors 65
    2.4.4 Implications for *In-situ* Calcite Dissolution Rates 68
  2.5 Conclusion 72
Chapter 3: A Near-Equilibrium Coupled Mechanistic Model for Calcite Dissolution in Seawater with 0, 14, and 28 millimolar Total Sulfate 74
  3.1 Introduction 74
  3.2 Experimental Methods 80
  3.3 Background and Modification of MyAMI Code 81

3.4 Implementation into PHREEQC 84
3.4.1 Comparison with CO2SYS 84
3.4.2 Choice of Surface Speciation Model 87
3.5 Results and Discussion 88
3.5.1 Dissolution Experiments with Variable [SO_{4T}] 88
3.5.2 Surface and Solution Speciation Calculations 90
3.5.3 Proposed Kinetic Model 93
3.5.4 Comparison of Model Fits in Seawater versus Freshwater 96
3.6 Summary and Conclusions 97
Chapter 4: *Rate Enhancement from Carbonic Anhydrase: Mechanistic Insights from Immobilization within Carbon Capture Reactors 99*
4.1 Introduction 99
4.2 Methods 101
4.2.1 Reactor Designs 101
4.2.2 CA Immobilization Strategies 103
4.2.3 MIMS Method for CA Activity and Lifetime Measurements 105
4.3 Results and Discussion 107
4.3.1 Fluidized Bed Reactors 107
4.3.2 Physical Immobilization of Hydrogels 111
4.3.3 Coupling CA to CPG Beads 115
4.4 Summary and Conclusions 119
Chapter 5: *Conclusions and Future Work 120*
Bibliography 123
Appendix A: Derivation of Surface Model Equations 146

LIST OF ILLUSTRATIONS

Figure 1.1: BET rates (mol/cm^2/s) versus 1-Ω at 21°C for 20-53µm (open circles) and 70-100µm (closed circles) size fractions, as well as 20-53µm grains with different treatments (see text for details). The majority of the data were collected using powders sieved in 18.2MΩ cm^{-1} water, but the different symbols show the consistency of our rates across a range of powder size fractions and rinse treatments. 5

Figure 1.2: (a) Raw dissolution vs. time of two different size fractions of 13C-labeled calcite at 1-Ω = 0.83, normalized by the total fraction of powder dissolved. Curves become linear after 24 hours and the slope of the subsequent data points is taken as the rate (dashed/solid lines in the figure). The 20-53µm size fraction dissolves more quickly than the 70-100µm size fraction ($2.3 \cdot 10^{-3}$ vs. $1.4 \cdot 10^{-3}$ g/g/day), but both yield the same rate when corrected for BET surface area ($1.8 \cdot 10^{-13}$ mol/cm^2/s). (b) Raw dissolution vs. time at constant 1-Ω = 0.80. Increasing the temperature increases dissolution rate non-linearly. 7

Figure 1.3: Comparison of calcite dissolution rates (mol/cm^2/s) plotted vs. 1-Ω (a) near equilibrium, and (b) in Log-Log 1-Ω space from 1>Ω>0. Dissolution in seawater behaves differently than in freshwater (black squares in b). The y-error bars reflect the error on the linear fit to the dissolution vs. time data from 24 to 72 hours and do not include the uncertainty in surface area. 8

Figure 1.4: Calcite dissolution rates (mol/cm^2/s) versus in-situ pH$_{total}$ calculated from CO2Sys using measured alkalinity and DIC pairs. Note that the dissolution rate at each temperature changes by nearly three orders of magnitude over 0.3 pH units. Seawater dissolution rates decrease sharply at a lower pH than in freshwater. 9

Figure 1.5: Comparison of calcite dissolution rates (mol/cm^2/s) in this study at 21°C versus previously published rates in freshwater (FW), seawater (SW), and artificial seawater (ASW) at 25°C. All data were taken directly from the published papers and were not adjusted to account for updated carbonate system equilibrium constants. Each study is normalized by BET surface area except for Cubillas et al. (2005), which is normalized by geometric surface area. The points from Berner & Morse (1974) combine the data for SW with 1.6 µmol/L phosphate and ASW with 0.5 µmol/L phosphate in Appendix Tables B and C, respectively. Data from Walter & Morse (1985) are for synthetic calcite and were taken from Fig. 1 of their paper and normalized using BET surface area from Table 3. 10

Figure 1.6: Rate vs. 1-Ω at 5 (a), 12 (b), 21 (c), and 37°C (d) overlaid with best-fit lines to the data before and after Ω = 0.75, not including data where Ω >0.9 (fitted values for *k* and *n* are listed in Table 1.1). The dashed lines in each panel show the expected behavior for a linear (*n*=1) dissolution rate law. The linear rate law is anchored by the rate constant at Ω=0, and greatly overestimates dissolution near equilibrium. . 12

Figure 1.7: Arrhenius plot of rate constants derived from far-from-equilibrium ($\Omega<0.75$) experiments. A linear fit to the data yields a slope of -3021±229 corresponding to an activation energy of 25±2 kJ/mol. 14

Figure 1.8: Simplified model of a dissolving calcite crystal where each cube represents a $CaCO_3$ unit cell. Numbered arrows demonstrate different dissolution mechanisms, while letters show surface features. At low driving forces, dissolution is limited to the retreat of pre-existing steps (1), kinks (a), and adatoms (b). Steps are frequently sourced from screw dislocations, but are only shown at edges here for simplicity. Defects such as edge-dislocations (c) impart strain on the crystal lattice, resulting in localized areas of excess surface energy. As the solution becomes more undersaturated, these areas become available for defect-assisted 2D dissolution (2). At even greater undersaturations, 2D dissolution occurs homogenously across the calcite surface (3) without the need for pre-existing defects. Both (2) and (3) produce 2D etch pits (d) that will propagate radially until they reach the edge of the mineral or encounter another etch pit and are eliminated 17

Figure 1.9: Expected data trends as the calcite surface transitions between dissolution mechanisms. Far from equilibrium (left panel), 2D etch pits open homogenously across the surface and the data are described by Eq. (1.4a). At intermediate driving forces, 2D dissolution may only proceed at defects (middle panel). Very near equilibrium, the solution driving force is only strong enough to support dissolution at pre-existing steps or screw dislocations (right panel). Data resulting from step retreat are described by Eq. (1.4b). Absolute rates of dissolution are slowest for step retreat, but the normalized rate curves upwards versus $|\frac{1}{\sigma}|$ as the solution approaches equilibrium. 20

Figure 1.10: The same data as in Figure 1.3, but recast as dissolution velocity (m/s) vs. $|\frac{1}{\sigma}|$ over the full range of undersaturations ($0<\Omega<0.99$). Saturation state increases from left to right. Rates at 5, 12, and 37°C "curve upwards" as Ω approaches equilibrium, indicating dissolution by retreat of pre-existing steps. Tick marks on the top axis show Ω in increments of 0.1, with an additional tick at 0.95 to emphasize the highly non-linear nature of $|\frac{1}{\sigma}|$ axis. 21

Figure 1.11: Dissolution velocities (m/s) at 5 (a), 12 (b), 21 (c), and 37°C (d) from $0<|\frac{1}{\sigma}|<25$ ($0<\Omega<0.96$). Saturation increases from left to right. All temperatures are fit to Eq. (1.4a) from $0<|\frac{1}{\sigma}|<3.5$. 12, 21, 37°C are fit to Eq. (1.4a) between $3.5<|\frac{1}{\sigma}|<25$ while 5°C is fit to Eq. (1.4b). The intercepts (stars on Y-axis) and slopes of the fits to Eq. (1.4a) are presented in Table 1.3. 25

Figure 1.12: Temperature dependence of kinetic and energetic parameters of calcite dissolution in seawater. (a) Change in the intercept (proportional to β and n_s) and (b) slope (proportional to α) of the fit to Eq. (1.4a) for homogenous ($0<|\frac{1}{\sigma}|<3.5$, triangles) and defect-assisted ($3.5<|\frac{1}{\sigma}|<25$, circles) dissolution. Lines for constant α

are plotted in (b) for comparison with the data. Fits to the data are presented in Table 1.4. 27

Figure 1.13: Arrhenius plots for the kinetic coefficient (a) and nucleation site density (b) derived from fits to Eq. (1.4a). (a) The slope of ln(β) versus 1/T is -2700±700, corresponding to an activation energy of detachment from kinks/steps of 22±6 kJ/mol. (b) The slope of ln(n_s) versus 1/T is $2.7\pm0.4\bullet10^4$, corresponding to a kinetic energy barrier to etch pit initiation of -230±30 kJ/mol. 31

Figure 2.1: A standard 1.7L Niskin bottle was modified for dissolution experiments. A chamber containing ^{13}C-labeled material sealed within mesh packets was affixed to the side, along with a recirculating pump and an aluminum pressure case to hold the batteries. The pump operates continuously and pushes water over the labeled material in the direction of the blue arrows. 45

Figure 2.2: The dissolution rates of labeled material at 21°C in Nuclepore mesh packets (triangles) and fully assembled Niskin reactors (circles) agree with dissolution rates of dispersed calcite (diamonds) and coccoliths (stars) in Supelco bags. Rate errors are smaller than the symbols. Inset: The time evolution of the δ^{13}C signal (normalized by percent of total mass dissolved for comparison) for dispersed powder and powder in Niskin reactors with dashed lines to guide the eye. 47

Figure 2.3: Example outputs from the model of Subhas et al. (2017) demonstrating that increased boundary layer volumes (V_{BL}) can cause dissolution signals to appear linear while expressing the same net rate (top three fits) Continuing to increase the boundary layer eventually inhibits dissolution (bottom fit). These outputs were generated using: $R_{Diss} = 5\cdot10^{-13}$ moles s^{-1}, R_{Diss}/R_{Precip} =1.12, Mass = 1.5 mg $CaCO_3$, Surface Area (SA)= 900 cm^2 g^{-1}, and varying boundary layer thickness (BL_T) from 10 μm to 20 mm to achieve the desired $V_{BL} = BL_T \cdot SA \cdot Mass$ 48

Figure 2.4: Example of how failed reactors were identified at Station 4. Background profiles of silica (squares) were determined prior to reactor deployment. Reactors were sampled for silica after recovery and were deemed successful (blue circles) if their measured silica concentration was within one standard deviation (± 1.5 μmol L^{-1}) of the background profile. Data from failed reactors (red circles) were easily identified and subsequently discarded. 51

Figure 2.5: Background profiles of δ^{13}C (squares) measured at (a) Station 2, (b) Station 3, (c) Station 4, (d) Station 5, each plotted with the δ^{13}C measured in the Niskin reactors upon recovery (circles). Station 5 points outlined in red were deployed after a storm (see text for details). Errors on δ^{13}C measurements are smaller than the points. The dashed horizontal lines show $\Omega_{(Alk,\ pH)}$ = 1 (black) and $\Omega_{(Alk,\ DIC)}$ = 1 (grey) with corresponding uncertainty. The offset between $\Omega_{(Alk,\ pH)}$ and $\Omega_{(Alk,\ DIC)}$ exceeded measurement error at Stations 3, 4, and 5. Dissolution was observed when supersaturated for $\Omega_{(Alk,DIC)}$ but undersaturated for $\Omega_{(Alk,\ pH)}$ (b, d). No dissolution occurred when supersaturated for $\Omega_{(Alk,\ pH)}$ (star, d). 53

Figure 2.6: (a) The difference between measured pH_T and calculated $pH_{T(Alk, DIC)}$ versus measured pH_T for data collected on CDisK-IV and a 2015-P16 cruise. (b) 2015-P16 pH offsets versus depth. 54

Figure 2.7: Dissolution rate (mol cm^{-2} s^{-1}) of synthetic calcite versus (a) 1-Ω and (b) Log(Rate) versus Log(1-Ω). Points are colored by their deployment depth, and reactors deployed after a storm at Station 5 are outlined in red. Error bars are plotted for both rate and Ω, but are frequently smaller than the symbols. 57

Figure 2.8: Comparisons of Log(Rate) (mol cm^{-2} s^{-1}) versus either Log(1-Ω) (a, c) or 1-Ω (b, d) for calcite dissolution experiments in the lab and *in-situ*. (a) Dissolution at 5°C in poisoned, filtered, UV-treated Dickson seawater (squares) versus dissolution measured *in-situ* in the N. Pacific (circles). The light grey circles are *in-situ* dissolution measurements made after the storm at Station 5. (b) Dissolution rates at 5°C in archived North Pacific seawater before (white triangles) and after (brown triangles) DIC increased by 152 μmol kg^{-1}. The arrow in (a) and (b) indicates a point at Log(1-Ω) = -3.3 which may be more clearly seen in the expanded version of this figure (Fig. S3). (c) Dissolution rates in Dickson seawater at 21°C (diamonds, from Naviaux et al. 2019) and with Dickson seawater spiked with different potential inhibitors. (d) The same as (c), but versus 1-Ω and with experiments conducted at 5°C. The point at Log(1-Ω) = -3.3 is left off of (d) for visual clarity. 59

Figure 2.9: Expanded version of Figure 2.8a of Log(Rate) (mol cm^{-2} s^{-1}) versus Log(1-Ω) for calcite dissolution experiments in the lab and *in-situ*. No dissolution was observed at Ω = 1.05 ± 0.02 in the lab, but dissolution did occur at Log(1-Ω) = -3.3. The point at Log(1-Ω) = -3.3 is within error of Ω = 0, but still serves to demonstrate a slight Ω dependence for dissolution rates very near equilibrium. 60

Figure 2.10: (a)-(d) Profiles showing the systematic offset between $\Omega_{(Alk, pH)}$ (from CDisK-IV and 2015-P16) and $\Omega_{(Alk, DIC)}$ (from GLODAP) at each station. The GLODAP profiles were derived from 2006-P16 cruise measurements (EXPOCODE: 325020060213) of Alk and DIC data flagged as "acceptable." Ω was calculated using the same CO_2 system parameters as discussed in the main text. GLODAP Alk and DIC were measured to better than ± 3 μmol kg^{-1}, corresponding with $\Omega_{(Alk, DIC)}$ ± 0.03. Measurement errors for $\Omega_{(Alk, pH)}$ are ± 0.005 and are not visible 62

Figure 2.11: (a) Log(Rate) (mol cm^{-2} s^{-1}) versus Log(1-Ω) for our lab and *in-situ* measurements. The fits to the data are from Table 2.2. (b) The normalized dissolution rate (m s^{-1}) versus $|\frac{1}{\sigma}|$. The x-axis is reversed from Naviaux et al. (2019) to ease comparison with (a). Tick marks are included at intervals of 0.1 Ω units, with one extra tick at Ω=0.95 to emphasize the non-linear nature of the $|\frac{1}{\sigma}|$ axis. Data from $20>|\frac{1}{\sigma}|>4.4$ (0.95>Ω>0.8) are fit to Eq. (2b) for dissolution by the retreat of pre-existing steps. Data from $4.4>|\frac{1}{\sigma}|>0$ (0.8>Ω>0) are fit to Eq. (2a) for dissolution by homogenous etch pit formation. Fitting parameters are in Table 2.3 63

Figure 2.12: Compilation of *in-situ* dissolution rates of inorganic calcite overlaid upon our measured lab and *in-situ* rates. The rate data from Honjo & Erez (1978) are from their Table 2 for reagent calcite and large calcite crystals, and Ω is from Takahashi (1975). Rate and Ω data for Troy et al. (1997) are from their Figure 12. Troy et al. documented dissolution above the saturation horizon, but these data are not included. Peterson (1966) rate data are from Fig. 2 of his paper, with Ω from 2015-P16 at a comparable location (see text for details, as well as Fig. S5). The shaded area represents theoretical bounds for dissolution in low DOC (top curve) and high DOC (bottom curve) seawater. The bounds are fit by the 5°C *n* and *k* values in Table 1. The lower bound is fit by $R=10^{-14.3\pm0.2}(1-\Omega)^{0.11\pm0.1}$ for $0.8 < \Omega < 1$, and $R=10^{-10.8\pm0.4}(1-\Omega)^{4.7\pm0.7}$ for $0 < \Omega < 0.8$. 70

Figure 2.13: (a) Estimates for the saturation state at the location of Peterson's (1966) moored calcite spheres. Ω estimates by Berner & Wilde (1972) are from their Table 2 and were based upon measurements of pH and carbonate alkalinity near Peterson's deployment site. Takahashi subsequently returned to the Peterson deployment site in 1973 and measured the total alkalinity, DIC, salinity, and temperature. The Takahashi data was taken from GLODAP v2 Bottle Data (Station ID: 33541, EXPOCODE: 318M19730822) and input into CO2SYS using the carbonate system parameters outlined in the main text. The resulting $\Omega_{(\mathrm{Alk,\ DIC})}$ is similar to the ΔpH profile in Fig. 8 published by Takahashi (1975), but our calculated Ω has a shallower slope versus depth. The profiles match to a depth of 3000 m, but we calculate Ω=0.7 at 5000 m compared with Takahashi Ω = 0.4 (ΔpH = 0.2, Fig. 8 of their paper). Given the issues with $\Omega_{(\mathrm{Alk,\ DIC})}$ discussed in the text, Peterson's data were plotted versus $\Omega_{(\mathrm{Alk,\ pH})}$ measured at the same latitude on a 2015 P16 cruise. (b) The P16 line was 20° East of the Peterson site, but the profile is similar in shape to the original Berner & Wilde estimate. Peterson documented dissolution from 500-2000 m, and these depths are undersaturated by P16 $\Omega_{(\mathrm{Alk,\ pH})}$, but supersaturated for Takahashi $\Omega_{(\mathrm{Alk,\ DIC})}$. 71

Figure 3.1: Data transcribed from Table 10 of Busenberg and Plummer (1986) on calcite dissolution rates (mol cm^{-2} s^{-1}) versus 1-Ω in $Ca(HCO_3)_2$ solutions at different pCO_2 levels. The n = 1 line is a fit to Rate = k(1-Ω) using a k of $9\cdot10^{-10}$ mol cm^{-2} s^{-1}. 78

Figure 3.2: (a) $\mathrm{Log_{10}}$Concentration versus pH_T in seawater at T=25°C, S=35, total DIC = 2 mM, for $[H_2CO_3^*]$, $[HCO_3^-]_T$, and $[CO_3^{2-}]_T$ calculated using the default PHREEQC database (red), and an updated database using the constants in Table 3.2 (blue). Empirical seawater pK^* values are included for reference. The equilibrium between each species is offset towards higher pH values when computed by the default PHREEQC database. (b) Ω_{CO2SYS} versus $\Omega_{\mathrm{PHREEQC}}$ calculated by different iterations of PHREEQC databases for DIC = 2 mM and varying pH_T. See text for details. (c) The offset between Ω calculations versus Ω_{CO2SYS}. Even with updated K_{sp}^*, the default PHREEQC database is over 0.15 Ω units offset from Ω_{CO2SYS}. The fully updated PHREEQC database agrees within 0.02 Ω units from $0 < \Omega < 1$ 86

Figure 3.3: Dissolution rate (mol cm^{-2} s^{-1}) of inorganic calcite at 21°C in Dickson seawater (diamonds, 28 mM SO_{4T}, from Naviaux et al. 2019) and Aquil with 28 mM SO_{4T} (dark grey) 14 mM SO_{4T} (grey) or 0 mM SO_{4T} (open circles) plotted as (a)

Log$_{10}$(Rate) vs. pH$_T$, (b) Log$_{10}$(Rate) vs. Log$_{10}$(1-Ω), (c) Rate vs. 1-Ω. Error bars are typically smaller than symbols. The 0 mM SO$_{4T}$ point closest to equilibrium is within error of 0 dissolution rate. 90

Figure 3.4: Log$_{10}$(Concentration) versus pH$_T$ for (a) solution carbon speciation in 28 (solid lines), 14 (large dashes), and 0 mM (small dashes) SO$_{4T}$ seawater and (b) mineral surface speciation in 28 (solid lines) and 0 mM SO$_{4T}$ seawater. Symbols indicate surface species present in Eq. 3.4. 91

Figure 3.5: Log$_{10}$(Concentration) versus Ω for (a) solution carbon speciation in 28 (solid lines), 14 (large dashes), and 0 mM (small dashes) SO$_{4T}$ seawater and (b) mineral surface speciation in 28 (solid lines) and 0 mM SO$_{4T}$ seawater. (c) the relative difference between species concentrations in 0 mM and 28 mM SO$_{4T}$ seawater versus Ω. Symbols indicate surface species present in Eq. 3.4. 92

Figure 3.6: Fits of Eq. 3.4 to experimental rate (mol cm^{-2} s^{-1}) versus 1-Ω data in (a) linear axes and (b) Log-Log axes. Dissolution in Dickson seawater is fit by the blue curve, 14 mM SO$_{4T}$ Aquil by the red curve, and 0 mM SO$_{4T}$ Aquil by the grey curve. Data near equilibrium is well described by the model (solid lines), but extrapolating the fit to Ω = 0 (dashed lines) systematically misfits dissolution rates. Note that the chatter in the fits near equilibrium is because net dissolution is the difference between large gross dissolution and gross precipitation fluxes which have been calculated using interpolated speciation data. 94

Figure 3.7: Contribution of each term of Eq. 3.4 to the overall dissolution rate in (a) Dickson seawater, (b) 14 mM SO$_{4T}$ Aquil, and (c) 0 mM SO$_{4T}$ Aquil. The “Net Rate” curves stop when the overall rate becomes negative. Horizontal dashed lines are provided to help see changes in the k_1 and k_6-k_3 terms between solution compositions. 96

Figure 4.1: Schematic of fluidized bed reactor (left) and full assembled reactor (right) ... 102

Figure 4.2: Custom 40 mL MIMS sample reactor (left) with hydrogel housing unit (right) 106

Figure 4.3: Increase in effluent alkalinity for fluidized bed reactors operating on a) 10% CO$_2$ in seawater (starting alk 1900 μmol kg^{-1}), b) 3% CO$_2$ from the Caltech powerplant smokestack in freshwater (FW, starting alk 1200 μmol kg^{-1}), c) Ambient air in freshwater. Reactors with 14 mg CA L^{-1} are in red. Dashed vertical lines indicate changes in the water inflow rate. Red vertical lines in c) indicate reactor structural failures (see text for details). 108

Figure 4.4: Amount of extra CO$_2$ captured (gCO$_2$ yr^{-1}) in reactors operating with 14 mg CA L^{-1} in freshwater versus the reactor overturning rate (hours, calculated from reactor volume divided by the water inflow rate). The relation follows an empirical power law dependence. 110

Figure 4.5: Representative CA-hydrogels a) cured in a 1 mL syringe using 2H2M photoinitiator with a $1\cdot10^{-3}$ W cm^{-2} 365 nm UV lamp and b) using LAP photoinitiator with a 1 W cm^{-2} 405 nm UV lamp. MIMS activity assays of c) ln(f^{18}) versus time of the same hydrogel tested over multiple days, and d) measured versus predicted activity for a hydrogel subdivided into smaller pieces. The dashed line in d) is the 1:1 measured:predicted activity based upon the increase in surface area from subdividing the hydrogel. 112

Figure 4.6: MIMS activity mgCA^{-1} over time of a suite of PEGDA-575 hydrogels relative to activity mg^{-1} of free CA (hydrogel activity / free CA activity). 114

Figure 4.7: CA-CPG beads dispersed in 50 mM pH 7 phosphate buffer (left) and sealed within 70 µm mesh bags (right) 116

Figure 4.8: Relative activity retention (measured activity / initial activity) of free CA (squares) and CA-CPG beads in 70 µm mesh bags (circles) versus time spent in solution bubbled with 10% CO_2 117

Figure 4.9: Total alkalinity versus time (left) for packed bed dissolution reactors (right). Two reactors were run in parallel at a flow rate of 3.2 mL min^{-1} of seawater. After an initial equilibration period, 1g of CA-CPG beads were mixed into Reactor 2 (pink coloring in the reactor in the right panel). When no change in alkalinity was observed, 15 mg L^{-1} of free CA was added to inflow streams of both reactors. 118

Figure 5.1: Comparison of dissolution rates inferred by Alk* measurements from Feely et al. (2002) with box model results for inorganic calcite dissolution at CDisK-IV Station 5 using the rate law from Chapter 2, a sinking rate of 1 m day^{-1}, and particle flux of 0.69 mmol m^{-2} day^{-1} (upper limit calcite flux from Dong et al. 2019). 121

Figure 5.2: Comparison of calcite dissolution rates (mol cm^{-2} s^{-1}) versus $\mathrm{Log}_{10}(1-\Omega)$ at 21°C published by our group. The Subhas et al. (2015) Ω values have been corrected from 25 to 21°C. All dissolution rates measured from July 2015-2017 have been faster than those measured prior to July 2015. These fast measurements were replicated independently by Dr. Subhas (July 2015) as well as during an inter-comparison study by each member in our group. They also include multiple different size fractions (20-53 and 70-100 µm) from different powder batches, as well as homegrown calcite (300-500 µm). 123

LIST OF TABLES

Table 1.1: York Fits to Log(R) = Log(k) + nLog(1-Ω) 11

Table 1.2: E_a Compilation for bulk calcite dissolution far from equilibrium 15

Table 1.3: Fits to Eq. (1.4a) for 2D Dissolution 26

Table 1.4: Coefficients for the Observed Temperature Effect 28

Table 1.5: Constants and calculated values for β, n_s and α 29

Table 2.1: Results from *in-situ* Dissolution Reactors. Alkalinity and pH_T measured to ± 3 μmol kg^{-1} and ± 0.001 units, respectively, resulting in Ω ± 0.005 units 56

Table 2.2: Fits to Empirical Rate Equation 63

Table 2.3: Fits to 2D Nucleation Equations 65

Table 3.1: Composition of "Aquil" Artificial Seawater 81

Table 3.2: Outputs from Mod-MyAMI Code. pK^* values are on the pH_T scale. γ^T and γ^F represents the "total" and "free" ion activity coefficients, respectively 84

Table 3.3: Comparison of surface binding constants among complexation models 88

Table 3.4: Best fit to rate constants in Eq. 3.4 when rate is expressed in mol cm^{-2} s^{-1} and surface species densities are in mol m^{-2} 93

Table 4.1: Summary of Hydrogel Materials 104

Table 4.2: Results from fluidized bed reactors 107

Table 4.3: Summary of Hydrogel Experiments 113

Table 4.4: Summary of CA-CPG Activity 116

Chapter 1

TEMPERATURE DEPENDENCE OF CALCITE DISSOLUTION KINETICS IN SEAWATER

1.1 Introduction

Carbonate dissolution has been extensively studied for decades, but the functional form of its kinetic rate law is still debated. The simplest formulation, and the one used most frequently in the oceanographic community, is based upon an assumption that calcite dissolves via attack of water at the surface:

$$\mathrm{CaCO_3 + H_2O \rightleftharpoons Ca^{2+} + CO_3^{2-} + H_2O} \qquad (1.1)$$

In transition state theory, the overall dissolution rate (R_{diss}) is the sum of simultaneous forward (R_f) and back (R_b) reactions, each with their own rate constants (k_f, k_b) such that:

$$\mathrm{R_{diss}} = R_f - R_b = k_f - k_b[Ca^{2+}]^m[CO_3^{2-}]^m \qquad (1.2a)$$

Here, m is a constant describing the stoichiometry of the dissolution reaction. The forward rate depends solely on k_f in this formulation, as the activity of the solid is assumed to be 1. Substituting in the definitions of $\frac{k_f}{k_b} = [Ca^{2+}]^m[CO_3^{2-}]^m = K_{sp}^m$ and $\Omega = \frac{[Ca^{2+}][CO_3^{2-}]}{K_{sp}}$ yields (Lasaga, 1998):

$$\mathrm{R_{diss}} = k_b K_{sp}^m - k_b[Ca^{2+}]^m[CO_3^{2-}]^m = k(1-\Omega^m) \qquad (1.2b)$$

Here, k is the net dissolution rate constant per unit area and $1\text{-}\Omega^m$ is a measure of the thermodynamic driving force of the solution. Absent of mechanistic understanding, the oceanographic community has historically fit dissolution rates using the empirical equation (Berner and Morse, 1974; Keir, 1980; Morse, 1978):

$$\mathrm{R_{diss}} = k(1-\Omega)^n \qquad (1.2c)$$

Here, n is referred to as the reaction order.

There is an ongoing conversation in the oceanographic community about whether calcite dissolution in natural waters obeys linear kinetics ($m=n=1$), or if a higher order n is required. The answer has important mechanistic implications, as values of n other than 1 imply that reactions beyond Eq. (1.1) set the dissolution rate of calcite in the ocean. Linear kinetics may be a reasonable approximation for synthetic calcite in non-seawater solutions (Svensson and Dreybrodt, 1992) far from equilibrium ($\Omega<0.8$, Cubillas et al., 2005) or with packed calcite beds (Boudreau, 2013; Sulpis et al., 2017), but results with suspended particles both in the laboratory (Gehlen et al., 2005; Keir, 1983, 1980; Morse and Berner, 1972; Subhas et al., 2015; Teng, 2004; Walter and Morse, 1985; Xu et al., 2012) and *in-situ* (Berelson et al., 2007, 1994; Fukuhara et al., 2008; Honjo and Erez, 1978; Peterson, 1966) have consistently reported non-linear relationships between dissolution rate and undersaturation. The discrepancy cannot be attributed solely to uncertainties in calcite's apparent solubility product (Hales and Emerson, 1997), as recent work using updated K_{sp} values has confirmed non-linear kinetics for synthetic (Dong et al., 2018; Subhas et al., 2015, 2017) and biogenic (Subhas et al., 2018) calcites at the near equilibrium undersaturations ($0.7<\Omega<1$) most relevant to the modern ocean water column (Olsen et al., 2016).

The oceanographic community has focused on the $(1-\Omega)^n$ rate law, but alternative theories dating back to Burton and Cabrera (1949; Burton et al., 1951; Cabrera and Levine, 1956) argue that the solution driving-force is a necessary, yet ultimately insufficient predictor of reaction kinetics. Crystals are made up of heterogeneous distributions of steps, kinks, defects, and dislocations, and their differing reactivities constrain both the rates and mechanisms of growth/dissolution. For example, it has been shown, using atomic force microscopy (AFM), that calcite dissolution in dilute solutions is limited to pre-existing steps until critical Ω thresholds are surpassed, at which point the overall rate increases dramatically as edge and screw dislocations open to become etch pits (Teng, 2004 and references therein). Models based upon the observed spread of 2D etch pits (Dove et al., 2008, 2005) or pulsing stepwaves (Fischer and Lüttge, 2018; Lasaga and Lüttge, 2001; Lüttge, 2006) allow for these mechanistic transitions and have been used to describe dissolution for a variety of minerals.

The temperature dependence of calcite dissolution kinetics has been extensively studied as a means to understand the mineral's dissolution mechanism, but no study has investigated this dependence in seawater. Knowledge of the elementary reactions and surface complexes responsible for dissolution (Arakaki and Mucci, 1995; Busenberg and Plummer, 1986; Chou et al., 1989; Plummer et al., 1978; Pokrovsky and Schott, 2002), and their respective activation energies (Plummer et al., 1978; Oleg S. Pokrovsky et al., 2009) is limited to simple non-seawater solutions far from equilibrium. It is generally agreed that the dissolution rate of calcite is linearly dependent on the concentration of H^+ for $pH<4$-5 (Plummer et al., 1978; Plummer et al., 1979; Busenberg and Plummer, 1986; Chou et al., 1989; Arakaki and Mucci, 1995; Alkattan et al., 1998), and that the activation energy for the reaction is on the order of 8-10.5 kJ/mol (Morse and Arvidson, 2002; Sjöberg and Rickard, 1984a). The dissolution mechanism becomes more complicated at higher pH values as the system enters a regime of mixed transport and surface reaction control (Rickard and Sjöberg, 1983; Sjöberg and Rickard, 1984a). Rate constants collected in the mixed control regime combine several processes, so bulk dissolution studies frequently report "apparent," rather than true activation energies. Apparent activation energies vary with solution composition and experimental design, but tend to range from 14-25 kJ/mol when measured under atmospheric pCO_2 levels (Finneran and Morse, 2009; Gledhill and Morse, 2006; Gutjahr et al., 1996; Sjöberg, 1978; Sjöberg and Rickard, 1984a). Apparent activation energies can reach as high as 60 kJ/mol at elevated pCO_2 (Oleg S. Pokrovsky et al., 2009). AFM studies can calculate activation energies for specific surface processes (Liang et al., 1996; Liang and Baer, 1997; MacInnis and Brantley, 1992; Xu et al., 2010), but dissolution rates derived from scaling up AFM measurements frequently disagree with those from bulk dissolution measurements (Arvidson et al., 2003; Morse et al., 2007)

The goal of our work is to provide the first measurements of the temperature dependence of calcite dissolution kinetics in seawater. Using the ^{13}C tracer method of Subhas et al. (2015), we dissolve labeled calcite powders in a closed system at 5, 12, 21, and 37°C across the full range of saturation states. Our experiments are conducted in filtered seawater, and the sensitivity of the ^{13}C tracer method allows us to resolve the near equilibrium Ωs most relevant to the ocean. We gain further insight by applying the surface nucleation model of Dove et al. (2005) to our data to identify changes in dissolution mechanism and to parse the near-equilibrium effects of temperature on the physical and energetic properties of calcite.

1.2 Methods

Following the methods of Subhas et al. (2015), ^{13}C labeled calcium carbonate powder was purchased from Sigma Aldrich (SKU 492027, >99 atom%) and wet sieved (solution information below) into 70-100 and 20-53 μm size fractions. The total specific surface areas for each fraction were determined by Kr gas BET to be 900±40 cm^2/g for the 70-100um fraction, and 1520±60 cm^2/g for the 20-53 μm fraction. Dissolution rates in the literature are frequently normalized by average geometric surface area (270 and 625 cm^2/g for our samples), but we use BET normalized rates as they produce a tighter agreement between our size fractions. The use of geometric surface area does not affect our results, and for comparison, both geometric surface area rates ($g/cm^2/day$) and mass normalized rates (g/g/day) are reported alongside our BET surface area rates in the Appendix (Table A1).

It has been shown that a mineral's reaction history can alter densities of steps, edges, and/or etch pits, thereby changing the dissolution rate that is eventually measured (Arvidson et al., 2003; Arvidson and Luttge, 2010; Fischer et al., 2014, 2012). To ensure that our dissolution rates were not an artifact of our choice of sieving liquid, we compared dissolution rates of powders sieved in: (1) pure 18.2MΩ cm^{-1} water, (2) 18.2MΩ cm^{-1} water adjusted to pH 8.5 with ammonium hydroxide, and (3) Dickson standard seawater (https://www.nodc.noaa.gov/ocads/oceans/Dickson_CRM/batches.html) adjusted to Ω≈1 via HCl addition. A subset of powder that had been sieved in pH 8.5 ammonium hydroxide was also baked at 80°C under vacuum for 7 days. No differences in subsequent dissolution rates were observed (Figure **1.1**), so data are reported for powders sieved in 18.2MΩ cm^{-1} water unless otherwise noted.

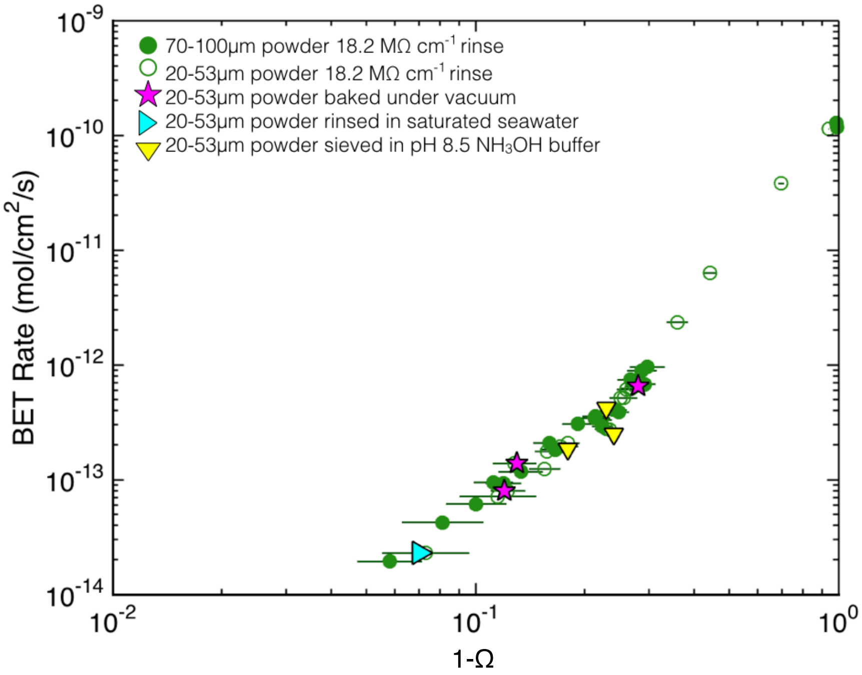

Figure 1.1: BET rates (mol/cm^2/s) versus 1-Ω at 21°C for 20-53μm (open circles) and 70-100μm (closed circles) size fractions, as well as 20-53μm grains with different treatments (see text for details). The majority of the data were collected using powders sieved in 18.2MΩ cm^{-1} water, but the different symbols show the consistency of our rates across a range of powder size fractions and rinse treatments.

Experimental bags were prepared by placing 1-5mg of Ca^{13}CO$_3$ powder inside a 1-L Supelco bag (part no. 30336-U) that had been modified (Subhas et al. 2015) to include an extra sampling port. The additional ports housed 0.2 μm filters to retain the carbonate powder during sampling. Bags were heat sealed and evacuated to remove all headspace. Experimental fill waters were made separately by first siphoning Dickson standard seawater (Batches 144-165) into another evacuated Supelco bag, and then titrating its total alkalinity (and therefore Ω) to the desired level via injection of 0.1M HCl. Silicate and phosphate differed between Dickson seawater batches, but only varied between 1-7 and 0.3-0.6

μmol/kg, respectively. Though phosphate adsorbs strongly to calcite surfaces (de Kanel and Morse, 1978; Millero et al., 2001) and is thought to be an inhibitor of dissolution (Berner and Morse, 1974; Sjöberg, 1978), variations in phosphate concentrations did not impact our results. The range of concentrations investigated in this study is much smaller than in studies that have documented significant inhibition (50 μmol/L, Walter and Burton, 1986), and preliminary experiments with seawater spiked to 20 μmol/L phosphate showed no inhibitory effect (not shown).

Each run began by siphoning 50g of fill water into the experimental bag to pre-rinse the calcite grains and remove any fine particles. The rinse water was subsequently taken out through the sampling port and discarded, after which the bags were filled with ~300g of seawater and placed in a recirculating water bath set to 5, 12, 21, or 37°C. The water bath maintained its temperature to ±0.1°C and was placed on a shaker table set to 85rpm. No change in dissolution rates were observed at higher shake speeds, but rates dropped significantly when stirring below 60rpm (Subhas et al., 2015). We used a rate of 85rpm to ensure that chemical transport was not limiting in our experiments. At no point was any headspace introduced into the system, so there was no change in the dissolved inorganic carbon (DIC) of the water due to exchange with the atmosphere. Fill water was always equilibrated to the desired temperature before being introduced into the experimental bags to ensure that initial measurements were not affected by a gradient in temperature between the bag and the water bath. Although not as important for experiments that ran for several days, this equilibration was crucial in achieving reproducible results in undersaturated waters below $\Omega<0.5$. Bags were sampled every 6-12 hours over the course of 2-5 days.

The samples were analyzed for DIC and ^{13}C using a Picarro cavity ringdown spectrometer. The $\delta^{13}C$ values were converted to moles dissolved per time, with typical traces shown in Figure **1**.**2**. The data become linear after an initial equilibration time <24 hours (Subhas et al., 2017), and points between 24 and 72 hours were fit with a linear regression using Microsoft Excel's Linest function, with the resulting slope taken as the dissolution rate. The relative error on the slope was used as the rate error and typically ranged from 1-5%. Total alkalinity was measured by open-system Gran titration and compared against the alkalinity expected from dissolution, as derived from the ^{13}C mass balance. The agreement between these alkalinities was always within 1-4 µmol/kg. The final saturation state was calculated by CO2SYS using measured DIC, total alkalinity, and temperature. Standard errors in DIC (±2-4 µmol/kg) and alkalinity (±1-3 µmol/kg) were propagated using a Monte Carlo approach, giving a final error on Ω of 0.01 to 0.04 units. We used the carbonate system dissociation constants from the Dickson and Millero (1987) refit to Mehrbach et al.'s (1973) data, sulfate dissociation constants from Dickson et al. (1990), and a borate to salinity ratio from Uppström (1974).

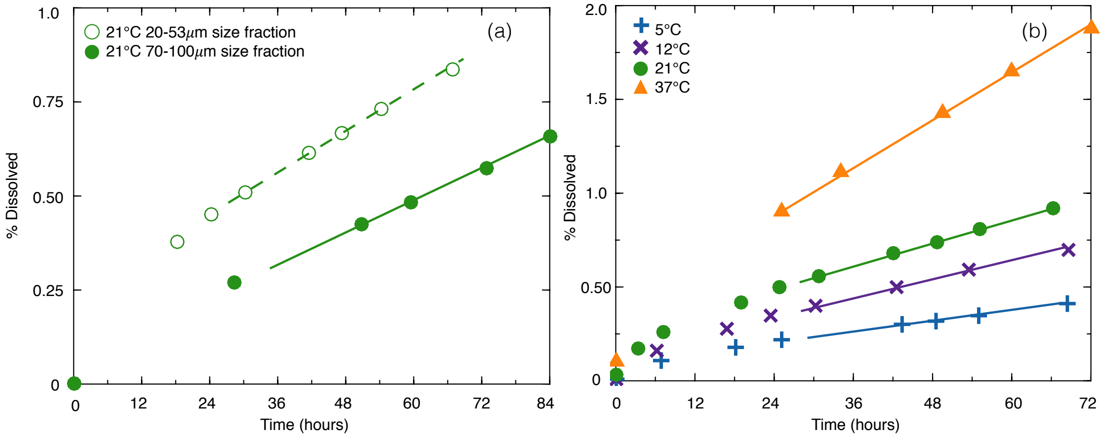

Figure 1.2: (a) Raw dissolution vs. time of two different size fractions of 13C-labeled calcite at $1\text{-}\Omega = 0.83$, normalized by the total fraction of powder dissolved. Curves become linear after 24 hours and the slope of the subsequent data points is taken as the rate (dashed/solid lines in the figure). The 20-53µm size fraction dissolves more quickly than the 70-100µm size fraction ($2.3\cdot10^{-3}$ vs. $1.4\cdot10^{-3}$ g/g/day), but both yield the same rate when corrected for BET surface area ($1.8\cdot10^{-13}$ mol/cm^2/s). (b) Raw dissolution vs. time at constant $1\text{-}\Omega = 0.80$. Increasing the temperature increases dissolution rate non-linearly.

Our dissolution rates were not affected by isotopic exchange. Experiments in supersaturated conditions (Ω=1.3) using the same methods saw no enrichment over the course of nine days beyond an initial increase in δ^{13}C of 1-3‰ (Subhas et al., 2015). Rate calculations rely on the rate of change of the $\delta^{13}C$ signal versus time, so the time independent exchange signal we observed does not alter our measurements of the net dissolution rate.

1.3 Results

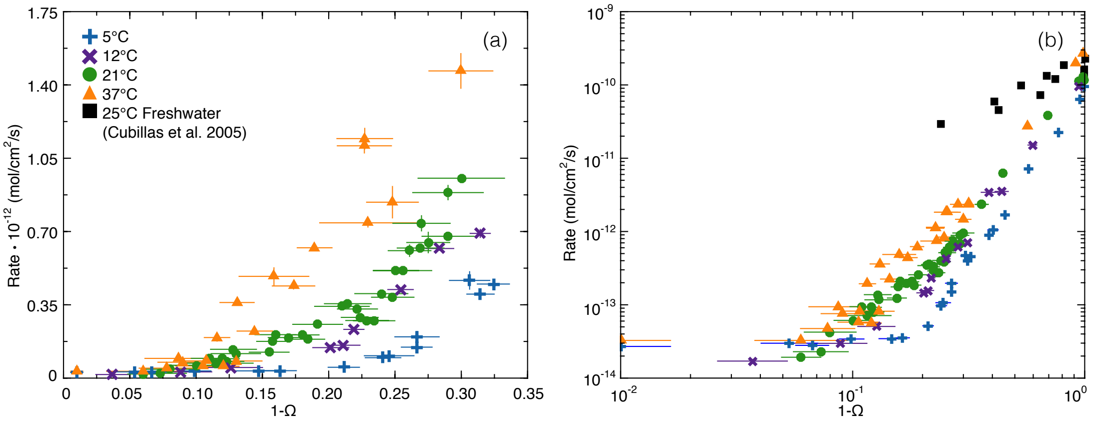

Figure 1.3: Comparison of calcite dissolution rates (mol/cm^2/s) plotted vs. 1-Ω (a) near equilibrium, and (b) in Log-Log 1-Ω space from 1>Ω>0. Dissolution in seawater behaves differently than in freshwater (black squares in b). The y-error bars reflect the error on the linear fit to the dissolution vs. time data from 24 to 72 hours and do not include the uncertainty in surface area.

Figure **1**.**3** shows our experimental results in the 1-Ω framework. Data in this plot cover a range of DIC and alkalinity of 1740-2050 and 807-2045 μmol/kg, respectively, corresponding with a calculated pH range of 5.7-7.65 on the total proton scale (Figure **1**.**4**). Our methodology allowed for rate data from each individual experiment to be collected under conditions of constant solution saturation and unchanging mineral surface area. Typical $\delta^{13}C$ dissolution signals were on the order of 5-40‰, where a 20‰ increase corresponds to a decrease in surface height of ~7-8 nm, an addition of just 1 μmol/kg of alkalinity, and the release of 10^{-7} mole of calcium (Subhas et al., 2015). This is the first work to measure the near-equilibrium temperature dependence of calcite dissolution with this level of sensitivity, and our analytical constraints mean that the observed rate changes may be more directly attributed to temperature dependent effects on the dissolution mechanism.

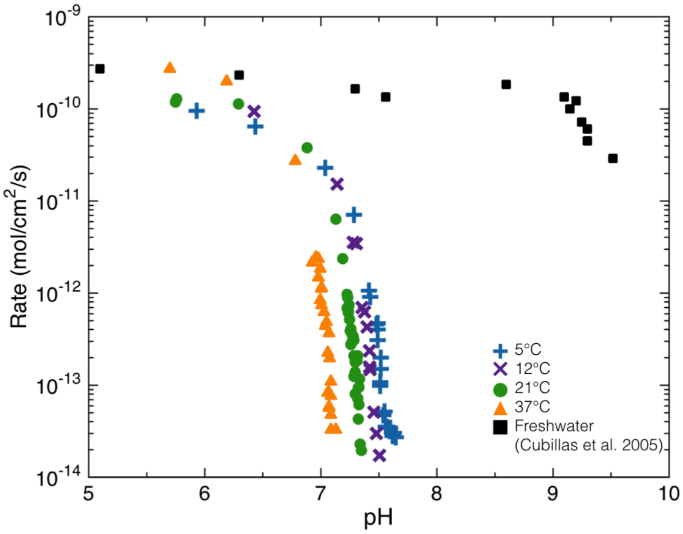

Figure 1.4: Calcite dissolution rates (mol/cm^2/s) versus in-situ pH$_{total}$ calculated from CO2Sys using measured alkalinity and DIC pairs. Note that the dissolution rate at each temperature changes by nearly three orders of magnitude over 0.3 pH units. Seawater dissolution rates decrease sharply at a lower pH than in freshwater.

We can see from Figure **1.3**b that, although calcite dissolves at a similar rate in freshwater (Cubillas et al., 2005) and seawater at $\Omega \approx 0$, the mineral responds fundamentally differently in each media to changes in saturation state. The dissolution rate in freshwater increases almost linearly as Ω drops (left to right on the plot), but seawater dissolution is highly non-linear at all temperatures and consists of multiple different slopes in log-log space. Our data show that calcite dissolution rates increase by four orders of magnitude as Ω decreases from 1 to 0.

Calcite dissolution kinetics in seawater respond to temperature in a complex manner. Dissolution rates appear least sensitive to temperature for Ω>0.9, but they transition to a regime where the temperature sensitivity increases greatly from 0.9>Ω>0.75. This strong dependence weakens after $\Omega \approx 0.75$, and the rate offsets between each temperature remain nearly constant as the solution approaches $\Omega = 0$.

1.4 Discussion

1.1.1 Analysis within the 1-Ω framework

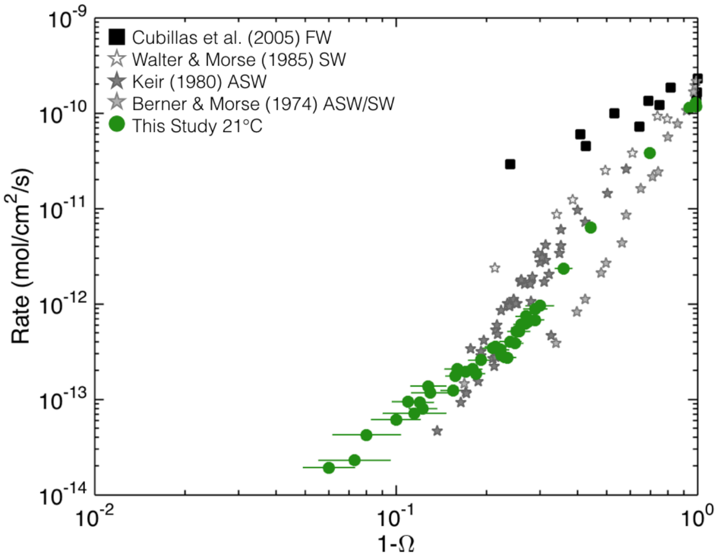

Figure 1.5: Comparison of calcite dissolution rates (mol/cm^2/s) in this study at 21°C versus previously published rates in freshwater (FW), seawater (SW), and artificial seawater (ASW) at 25°C. All data were taken directly from the published papers and were not adjusted to account for updated carbonate system equilibrium constants. Each study is normalized by BET surface area except for Cubillas et al. (2005), which is normalized by geometric surface area. The points from Berner & Morse (1974) combine the data for SW with 1.6 µmol/L phosphate and ASW with 0.5 µmol/L phosphate in Appendix Tables B and C, respectively. Data from Walter & Morse (1985) are for synthetic calcite and were taken from Fig. 1 of their paper and normalized using BET surface area from Table 3.

Previous work in freshwater has successfully fit calcite dissolution kinetics with near-linear rate laws (Cubillas et al., 2005; Svensson and Dreybrodt, 1992), but it is clear that this approach cannot describe our seawater data. Our results are highly non-linear against 1-Ω and exhibit a similar trend far from equilibrium as observed in previous bulk dissolution experiments in seawater (Figure **1.5**). Consistent with reports of a near equilibrium Ω_{crit} value in seawater (Dong et al., 2018; Subhas et al., 2015, 2017), we observe an abrupt change in the dissolution rate response to saturation at every temperature at $\Omega \approx 0.75$. Due to this change, no single rate law of the traditional $k(1\text{-}\Omega)^n$ form can describe the dissolution rate of calcite across the full range of saturation states. York regression fits to the reaction orders (n)

and net dissolution rate constants (*k*) are therefore calculated for data Ω<0.75 and Ω>0.75, with the results plotted in Figure **1.6** and listed in Table 1.1.

Table 1.1: York Fits to Log(R) = Log(k) + nLog(1-Ω)

T (°C)	Ω > 0.75		Ω < 0.75	
	$\text{Log}_{10}k$ (mol/cm^2/s)	n	$\text{Log}_{10}k$ (mol/cm^2/s)	n
5	-13.07 ± 0.18	0.34 ± 0.09	-10.01 ± 0.10	4.81 ± 0.07
12	-11.51 ± 0.15	1.92 ± 0.07	-9.95 ± 0.27	4.09 ± 0.15
21	-11.06 ± 0.10	2.15 ± 0.05	-9.83 ± 0.12	4.18 ± 0.07
37	-10.50 ± 0.13	2.47 ± 0.05	-9.56 ± 0.35	4.58 ± 0.22

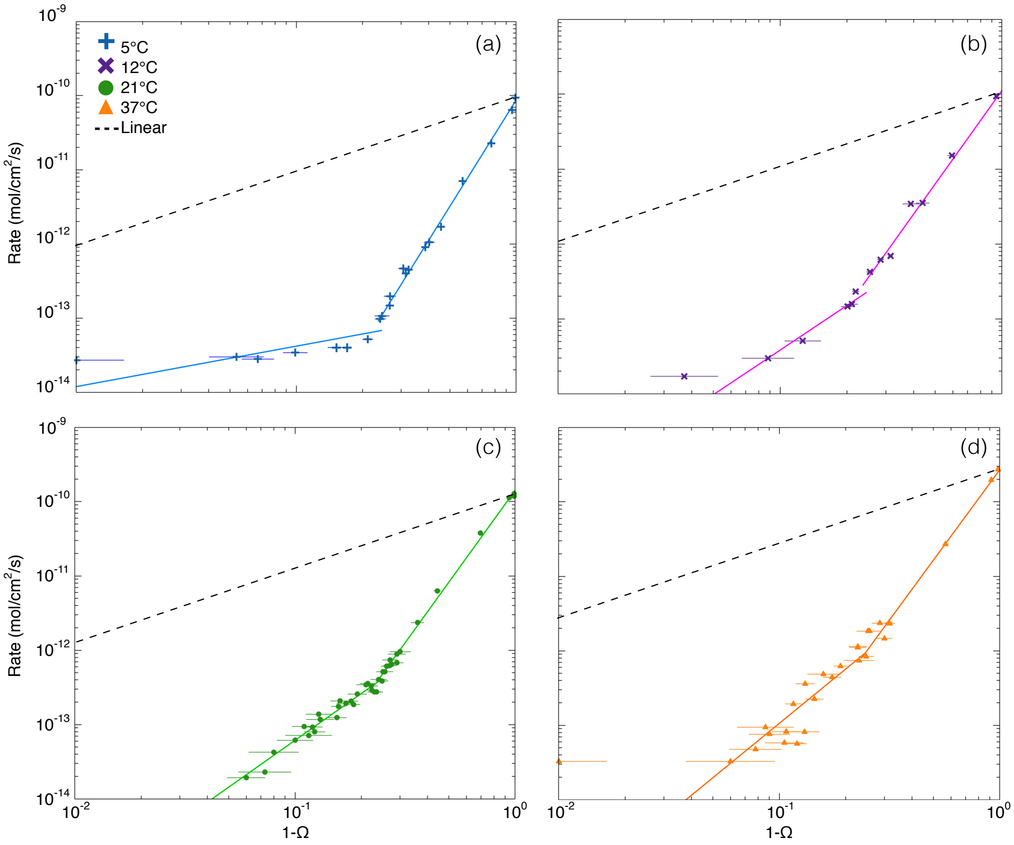

Figure 1.6: Rate vs. 1-Ω at 5 (a), 12 (b), 21 (c), and 37°C (d) overlaid with best-fit lines to the data before and after Ω = 0.75, not including data where Ω >0.9 (fitted values for *k* and *n* are listed in Table 1.1). The dashed lines in each panel show the expected behavior for a linear (*n*=1) dissolution rate law. The linear rate law is anchored by the rate constant at Ω=0, and greatly overestimates dissolution near equilibrium.

The deeply undersaturated (Ω<0.75) rate constants agree with values typically reported for calcite in solutions above pH >5 under atmospheric pCO_2 (order $1\cdot10^{-10}$ mol/cm^2/s, Plummer et al., 1978; Keir, 1980; Sjöberg and Rickard, 1985; Cubillas et al., 2005; Fischer and Lüttge, 2018; see also Table 5 in Subhas et al., 2015), and may be used to plot the expected behavior for a linear rate law by inserting them into Eq. (1.2c) with *n*=1 (the dashed lines in Figure **1.6**). In the region near equilibrium that is most relevant to the modern ocean (Ω>0.7), linear kinetics overestimate our measured rates by more than two orders of magnitude. The use of smaller *k*s would reduce the difference between the calculated and actual rates near saturation, but the resulting fit would be entirely empirical and no longer grounded in the theory behind the 1-Ω rate law. Imposing linear kinetics also guarantees that dissolution rates across large ranges of Ω will be systematically over or underestimated. Our near equilibrium data require the reaction order to change with temperature from 0.34 to 2.47, and the rate constant to increase by over two orders of magnitude. These changes are interesting, but they represent simple curve fits and do not allow for meaningful mechanistic interpretations.

The temperature dependence of the far-from-equilibrium ks may still be used to gain insight into the dissolution mechanism. The apparent activation energy (E_a) of the dissolution reaction can be evaluated using the Arrhenius relation:

$$\ln(\mathrm{k}) = \ln(A) - \frac{E_a}{R} \cdot \frac{1}{T} \tag{1.3}$$

Here, A is a pre-exponential factor (mol/cm^2/s), E_a is the apparent activation energy (kJ/mol), and R is the molar gas constant (kJ/mol/K). Plotting the far-from-equilibrium rate constants in Arrhenius space (Figure **1**.**7**) yields a value for E_a/R of -3021±229, corresponding to an apparent activation energy of 25±2 kJ/mol. This E_a agrees with results of previous studies in which calcite was dissolved in low pCO_2 media (Table 1.2), suggesting a common mechanism controls far-from-equilibrium dissolution regardless of the solution.

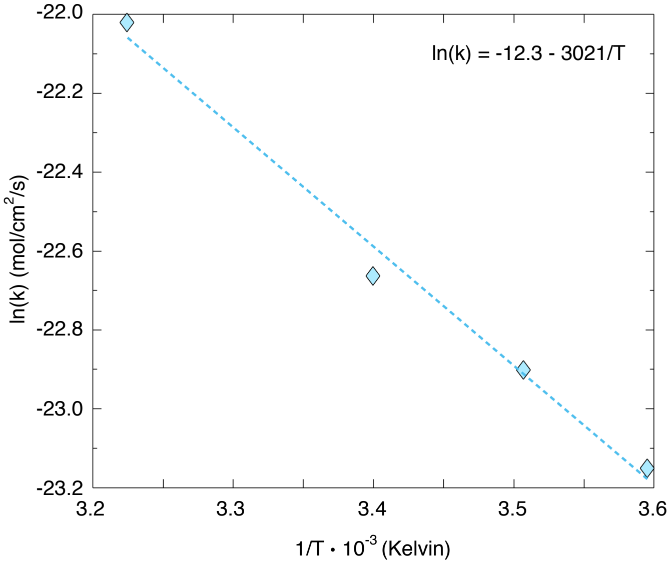

Figure 1.7: Arrhenius plot of rate constants derived from far-from-equilibrium ($\Omega<0.75$) experiments. A linear fit to the data yields a slope of -3021±229 corresponding to an activation energy of 25±2 kJ/mol.

Table 1.2: E_a Compilation for bulk calcite dissolution far from equilibrium

Study	Solution	Temperature (°C)	pH	Ω	Activation Energy (kJ/mol)
Plummer et al., (1978)	DI Water	5-60	2-5	0*	8.4 (from Eq. 5)
Salem et al., (1994)	DI Water	15-35	9.2	0-0.04	8.7
Sjöberg (1978)	0.7M KCl	3-50	3.0	0*	10.5 (crystal)
Sjöberg & Rickard (1984)	0.7M KCl	1-62	2.7-3.7	0*	13±1 (Iceland Spar, from Fig. 7)
Finneran & Morse (2009)	0.07-5M Ionic Media	25-85	5.5-6.5	0.4-0.8	20±2
Gledhill & Morse (2006)	50-200g/L Brine	25-82.5	5-6.2	0.2-1	21±1
Gutjahr et al. (1996)	Ionic NaCl	20-70	7-9	0.4-1	24±3 (k_{diss} from Table 2)
Sjöberg (1978)	0.7M KCl	3-50	8.3	0*	25.7 (crystals) 35 (powder)
Sjöberg & Rickard (1984)	0.7M KCl	1-62	8.4	0*	31-36 (Carrara Marble, Eq. 9)
Pokrovsky et al. (2009)	0.1M NaCl, (pCO_2 2-50atm)	25-100	4.0	0*	48.2±4.6**
This study	Natural Seawater	5-37	5.5-6.5	0-0.75	25±2

*Ω is not reported, but the solution composition suggests Ω=0

**Pokrovsky et al. (2009) adjust this E_a to 14.7±3.5 when correcting for chemical transport

Calcite dissolution is linearly dependent on the concentration of H^+ for pH<4-5, is transport limited, (Alkattan et al., 1998; Arakaki and Mucci, 1995; Busenberg and Plummer, 1986; Chou et al., 1989; Plummer et al., 1979a, 1978), and exhibits a relatively small activation energy (8-10.5 kJ/mol Sjöberg and Rickard, 1984; Morse and Arvidson, 2002). Larger activation energies, like those compiled in Table 1.2 generally seen at higher pHs, indicate that dissolution is not purely transport limited and that additional reactions are occurring at the mineral surface (Morse and Arvidson, 2002; Sjöberg and Rickard, 1983). The exponential rate law (Eq. 1.2c) is a statement of mechanism if the dissolution rate is linear

(n=1) versus undersaturation, but our data clearly show that n varies with Ω. Given the magnitude of the E_a and the strong non-linearity of our data, a different mechanistic framework is required to understand the near-equilibrium dissolution rate of calcite in seawater.

1.4.1 Identification of changes in dissolution mechanism

As did Subhas et al. (2017), we applied a mechanistic framework originally developed for crystal growth (Chernov, 1984; Malkin et al., 1989) that was subsequently and successfully adapted by Dove et al. (2005, 2008) to describe dissolution. Dove et al.'s work is based upon AFM observations of silica minerals dissolving at different solution undersaturations. The authors saw three distinct dissolution mechanisms: retreat of pre-existing steps at edges and screw dislocations near equilibrium, opening of 2D "pancake" etch pits at defects farther from equilibrium and, finally, opening of 2D etch pits homogenously across the mineral surface at deeper undersaturations (see schematic in Figure **1.8**). The onset of each mechanism was accompanied by an increase in dissolution rate. The same general transitions observed by Dove et al. (2005) for quartz dissolution also occur in the non-seawater dissolution of calcite (Teng, 2004), although the size and shape of calcite etch pits can differ from 2D "pancakes" due to interactions with ions in solution (Ruiz-Agudo and Putnis, 2012; Klasa et al., 2013 and references therein). Other calcite dissolution models have been proposed (Fischer et al., 2012; Lasaga and Lüttge, 2001), but we continue with the Dove framework because it allows for the identification of dissolution mechanisms from bulk rate data and it can parse the effects of temperature on various kinetic and energetic parameters.

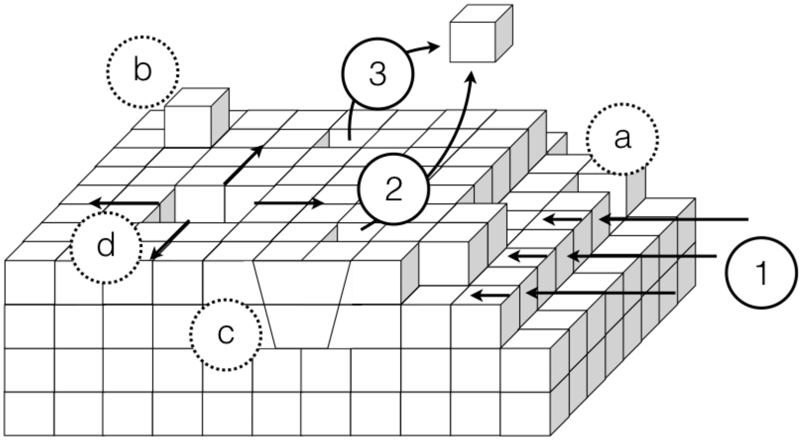

Figure 1.8: Simplified model of a dissolving calcite crystal where each cube represents a $CaCO_3$ unit cell. Numbered arrows demonstrate different dissolution mechanisms, while letters show surface features. At low driving forces, dissolution is limited to the retreat of pre-existing steps (1), kinks (a), and adatoms (b). Steps are frequently sourced from screw dislocations, but are only shown at edges here for simplicity. Defects such as edge-dislocations (c) impart strain on the crystal lattice, resulting in localized areas of excess surface energy. As the solution becomes more undersaturated, these areas become available for defect-assisted 2D dissolution (2). At even greater undersaturations, 2D dissolution occurs homogenously across the calcite surface (3) without the need for pre-existing defects. Both (2) and (3) produce 2D etch pits (d) that will propagate radially until they reach the edge of the mineral or encounter another etch pit and are eliminated

The exponential 1-Ω framework only considers the solution saturation state, but the Dove framework allows for changes in dissolution mechanism and incorporates information about a crystal's physical and energetic properties. This information is encapsulated in two equations describing the three different dissolution mechanisms: one equation for the spread of 2D etch pits, and one for the retreat of pre-existing steps. Recent observations have demonstrated that etch pits spread via pulsing stepwaves in deeply undersaturated solutions, and that the speed of the wave varies with the distance from its source (Fischer and Lüttge, 2018; Lasaga and Lüttge, 2001). The Dove rate equations make the simplifying assumption that the step speed does not depend on the source, and therefore uses a single equation to describe both defect-assisted and homogenous dissolution. This assumption is likely valid for bulk dissolution, as step speeds converge on a constant value within a new nanometers from the pit source (Fischer and Lüttge, 2018). Full derivations of the Dove equations may be found in the appendix. The overall rate of dissolution by either defect-assisted or homogenous 2D etch pit growth (*R_{2D}*) is given by:

$$\ln\left(\frac{R_{2D}}{(1-\Omega)^{\frac{2}{3}}|\sigma|^{\frac{1}{6}}}\right) = \ln\left(h\beta C_e(\omega^2 h n_s a)^{\frac{1}{3}}\right) - \frac{\pi\alpha^2\omega h}{3(k_b T)^2}\left|\frac{1}{\sigma}\right| \qquad (1.4a)$$

Here, the left hand term is now the normalized dissolution velocity (m/s), $|\sigma|=\ln(\Omega)$ is a measure of the solution driving force, h is the step height (m), β is the rate constant for surface retreat (step kinetic coefficient, m/s), ω is the molecular volume (m^3), n_s is the density of active nucleation sites (sites/m^2), a is the lattice spacing (m), α is the step edge free energy (mJ/m^2), k_b is Boltzmann's constant, T is the temperature (Kelvin), and C_e is the mineral solubility. The rate equations were derived for a single component crystal, so C_e has units of molecules/m^3. Calcite is a two component crystal, but we relate calcite K_{sp} (mol^2/kg^2) in seawater to C_e by assuming constant $[Ca^{2+}]$=0.01M, such that $K_{sp}/[Ca^{2+}]=C_e$ after converting from mol/kg to molecules/m^3.

Although it appears complex, Eq. (1.4a) describes a straight line with a slope set by a single term (the step edge free energy, α), and an intercept set collectively by the kinetic coefficient (β) and the number of active nucleation sites (n_s). All other terms are either fundamental mineral properties assumed to be constant (h, ω, a), or are determined by the experimental conditions (C_e, T, Ω, σ).

Dissolution by the retreat of pre-existing steps and screw dislocations (R_{step}) is given by a different equation:

$$\ln\left(\frac{R_{step}}{(1-\Omega)^{\frac{2}{3}}|\sigma|^{\frac{1}{6}}}\right) = \ln\left(\frac{\omega\beta C_e mh}{P}\right) + \ln\left((1-\Omega)^{\frac{1}{3}}\left|\frac{1}{\sigma}\right|^{\frac{1}{6}}\right) - \ln\left(1 + 8\left(\frac{\omega\alpha}{Pk_bT}\right)\left|\frac{1}{\sigma}\right|\right) \tag{1.4b}$$

Here, the added terms are the number of elementary steps (*m*, order 1) and the perimeter of the screw dislocation core sourcing the steps (*P*, proportional to 2*πmh*).

An advantage of this model is that bulk rate data exhibit distinct slopes when plotted as normalized rate versus $\left|\frac{1}{\sigma}\right|$ (Figure **1.9**), depending on the dominant dissolution mechanism. Even though both homogenous and defect-assisted dissolution are fit by Eq. (1.4a), we can distinguish between them based upon the distance from equilibrium. By definition, homogenous dissolution has a greater number of nucleation sites than defect-assisted dissolution. Data collected during homogenous dissolution are therefore expected to have a greater y-intercept than for defect-assisted dissolution. Additionally, we would expect the defect-assisted mechanism to have a shallower slope versus $\left|\frac{1}{\sigma}\right|$, as defects impose strain on the calcite surface and locally decrease the free energy of step formation per unit step height (α). The step-retreat mechanism is described by equation (1.4b), and curves upwards versus $\left|\frac{1}{\sigma}\right|$. Under this set of equations, it is important to note that the *absolute* rate always decreases as the solution approaches equilibrium (Figure **1.6**), and it is only the *normalized* rate that increases. The apparent increase near equilibrium is driven by the third term in Eq. (1.4b), where we take the natural log of (1-$\left|\frac{1}{\sigma}\right|$) (α is negative), and $\left|\frac{1}{\sigma}\right|$ becomes very large, and ultimately undefined, as Ω approaches 1.

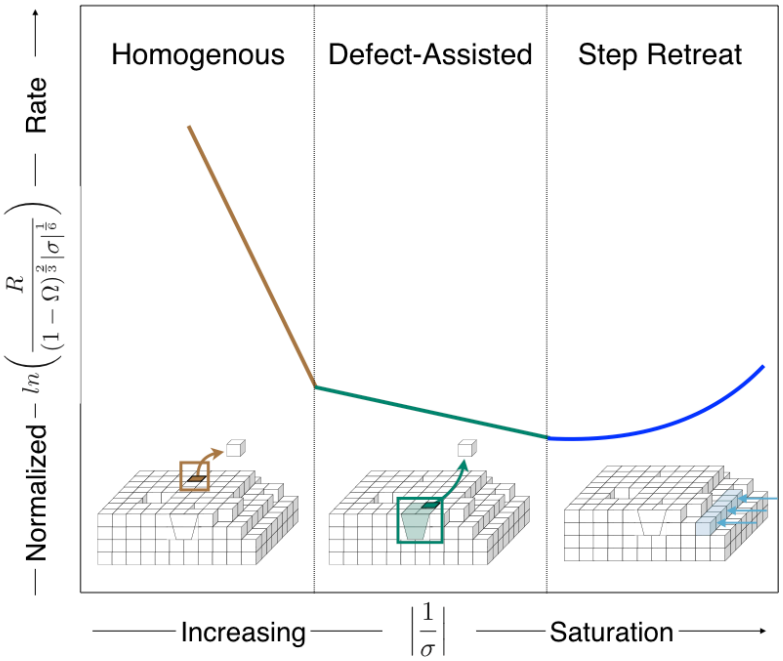

Figure 1.9: Expected data trends as the calcite surface transitions between dissolution mechanisms. Far from equilibrium (left panel), 2D etch pits open homogenously across the surface and the data are described by Eq. (1.4a). At intermediate driving forces, 2D dissolution may only proceed at defects (middle panel). Very near equilibrium, the solution driving force is only strong enough to support dissolution at pre-existing steps or screw dislocations (right panel). Data resulting from step retreat are described by Eq. (1.4b). Absolute rates of dissolution are slowest for step retreat, but the normalized rate curves upwards versus $\left|\frac{1}{\sigma}\right|$ as the solution approaches equilibrium.

Our results are plotted across the full range of saturations in Figure **1.10**, and they demonstrate each of the three expected trends in the surface framework. The non-linear nature of the x-axis emphasizes data collected at $\Omega>0.95$, so the axis is truncated from $0<\left|\frac{1}{\sigma}\right|<25$ ($0<\Omega<0.96$) in Fig. 8a-d to help view the data and fits more clearly. All temperatures exhibit a steep linear slope where $\left|\frac{1}{\sigma}\right|<3.5$ ($\Omega<0.75$). Closer to equilibrium, dissolution at 12, 21, and 37°C shifts to a shallower linear slope, but this is not observed in the 5°C data. Experimental dissolution rates measured at 12 and 37°C begin to 'curve upwards' after $\left|\frac{1}{\sigma}\right|$>10 (Ω>0.9, see also Figure **1.10**).

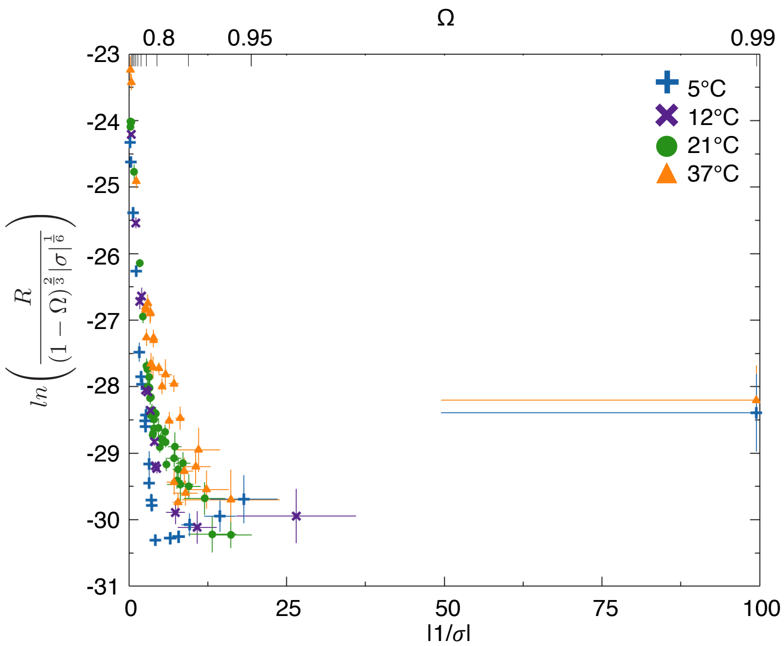

Figure 1.10: The same data as in Figure 1.3Figure 1.4, but recast as dissolution velocity (m/s) vs. $\left|\frac{1}{\sigma}\right|$ over the full range of undersaturations (0<Ω<0.99). Saturation state increases from left to right. Rates at 5, 12, and 37°C "curve upwards" as Ω approaches equilibrium, indicating dissolution by retreat of pre-existing steps. Tick marks on the top axis show Ω in increments of 0.1, with an additional tick at 0.95 to emphasize the highly non-linear nature of $\left|\frac{1}{\sigma}\right|$ axis.

We interpret each of the slope changes as mechanistic transitions that occur as the solution approaches equilibrium and falls below two critical energy barriers. Seawater calcite dissolution is dominated by homogenous etch pit formation from Ω=0 to Ω≈0.75, at which point etch pit formation may only occur at defects. These defect-assisted etch pits set the dissolution rate between Ω≈0.75 and Ω≈0.9, and dissolution at higher saturation states may only occur at pre-existing steps on edges and at screw dislocations. At 5°C, dissolution appears to skip over the defect-assisted mechanism and instead transitions directly to the step-retreat mechanism.

The critical Ωs for mechanistic transitions that we have identified in seawater are much closer to equilibrium than they are in freshwater. Compared to observations by Teng (2004) in weak electrolyte solutions, the Ω_{crit} for the opening of defect-assisted etch pits in seawater is $\Omega=0.9$ versus $\Omega=0.54$, and the Ω_{crit} for homogenous etch pit formation (defined by Teng as Ω_{max}) is $\Omega=0.75$ versus $\Omega=0.007$. The rate of seawater calcite dissolution will be set by the density of pre-existing steps for $\Omega>0.9$, and by the defect-density for $\Omega_{crit}>\Omega>\Omega_{max}$ ($0.9>\Omega>0.75$). At colder temperatures relevant to the deep ocean, dissolution will be set by the density of pre-existing steps for $1>\Omega>0.75$. Once homogenous 2D dissolution is activated at $\Omega<\Omega_{max}$ ($\Omega<0.75$), the overall rate will be limited by the maximum pit spreading rate.

The shift of calcite-seawater mechanistic transitions towards equilibrium is significant because it means that any model based upon a single rate equation, regardless of its reaction order, will not accurately capture dissolution responses to changes in saturation state. Our results suggest that typical ocean water column Ωs (>0.7) and temperatures (≤5°C) currently limit calcite to dissolution at pre-existing steps, but the oceans are acidifying due to fossil fuel burning and lowering both calcite and aragonite saturation states (Byrne et al., 2010; Doney et al., 2009; Feely et al., 2012, 2004). These perturbations in Ω may activate new surface mechanisms and elicit highly non-linear dissolution responses, both due to absolute changes in Ω and as regions where $\Omega<1$ occur in warmer waters. As a rough comparison, we can calculate the magnitude of the offset between oceanographic models that assume linear ($n=1$) kinetics for Eq. (1.2c) (Dunne et al., 2012; Hales and Emerson, 1997; Ilyina and Zeebe, 2012) and our 5°C data. Arbitrarily beginning with a total alkalinity of 2230 μmol/kg at surface pressure, calcite is saturated ($\Omega=1$) at a pH of ~7.6 at 5°C. Decreasing the pH by 0.1 units lowers Ω from 1.0 to ~0.8, maintaining step retreat as the rate-determining mechanism at 5°C and minimally affecting calcite dissolution rates. Further decreasing pH by 0.1 units drops Ω from ~0.8 to ~0.65, activating homogenous dissolution of the calcite surface. This second pH drop would increase calcite dissolution rates by a factor of ~25, whereas linear kinetics would predict only a factor of ~2. The discrepancy between the different rate laws will only widen as the oceans continue to acidify.

Models based upon the non-linear n=4.5 reaction order from Keir (1980) (Archer, 1996, 1991; Archer et al., 2009; Berelson et al., 1994; Jahnke et al., 1994; Jansen et al., 2002) are similarly inadequate to describe dissolution. The high reaction order employed in these models is only applicable for $0<\Omega<0.75$ (Table 2) and does not capture the change in dissolution response when transitioning mechanisms near equilibrium. We find that the dissolution rate at 5°C is relatively constant versus Ω for $1>\Omega>0.75$, so a reaction order of n=4.5 will correctly predict far-from-equilibrium dissolution while systematically underestimating rates near equilibrium. A more appropriate approach would be to employ two different rate equations at 5°C, one for step retreat $\Omega>0.75$, and one for homogenous dissolution $\Omega<0.75$. This recommendation maintains the simplicity of the empirical rate equation while accounting for changes in dissolution mechanism.

1.4.2 Using temperature dependence to extract physical and energetic parameters of calcite dissolution in seawater

The inherent variability in step and defect densities between minerals complicate rate comparisons between studies (Arvidson et al., 2003; Fischer et al., 2014), but we can still advance our knowledge of calcite dissolution kinetics by analyzing the temperature dependence of our results within the surface framework. All of our calcite powders were sourced from the same batch and may be presumed to have the same initial step and defect densities. Tight control of solution saturation means that dissolution rate changes within each mechanistic regime may be directly related to the temperature dependence of fundamental physical and energetic properties in the calcite-seawater system. We step through each mechanism and calculate step edge free energies (α), kinetic coefficients (β), and active nucleation site densities (n_s). We also use the temperature dependencies of β and n_s to estimate the activation energy for detachment from retreating steps (ϵ_{step}) and the kinetic energy barrier for removing an ion to initiate an etch pit (ϵ_{init}).

The fitted slopes and intercepts (Figure **1.11**) are resolved for both homogenous and defect-assisted etch pit formation (Table 1.3); the cutoff of each fit is set to $\left|\frac{1}{\sigma}\right|$=3.5 (Ω=0.75) to remain consistent with our analysis in the 1-Ω framework. Our results are not sensitive to the precise cutoff choice. As noted in Section 1.4.1, dissolution at 5°C appears to skip over the defect-assisted mechanism, so only $\left|\frac{1}{\sigma}\right|$<3.5 for the 5°C data is included in our analysis of etch pit dissolution. The 5°C data have the highest density of measurements near equilibrium, so it will be used later to evaluate the energetics of the step retreat mechanism.

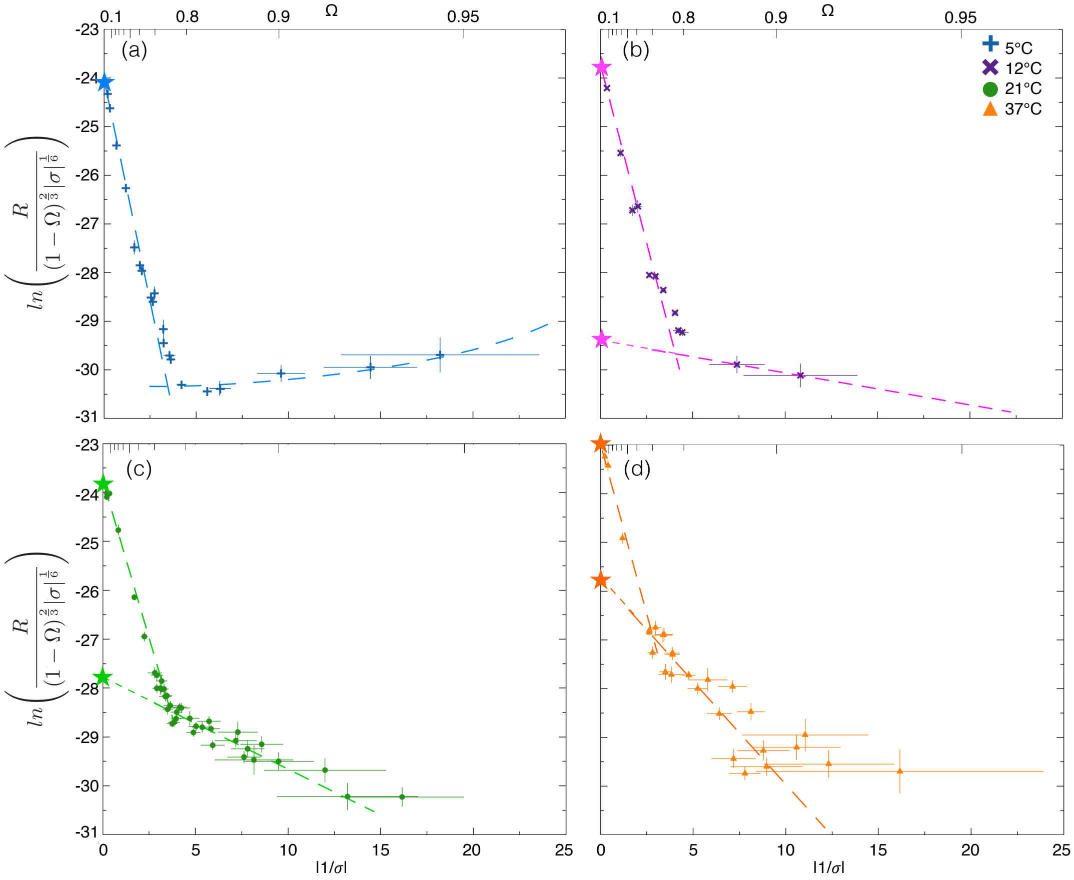

Figure 1.11: Dissolution velocities (m/s) at 5 (a), 12 (b), 21 (c), and 37°C (d) from 0<$\left|\frac{1}{\sigma}\right|$<25 (0<Ω<0.96). Saturation increases from left to right. All temperatures are fit to Eq. (1.4a) from 0<$\left|\frac{1}{\sigma}\right|$<3.5. 12, 21, 37°C are fit to Eq. (1.4a) between 3.5<$\left|\frac{1}{\sigma}\right|$<25 while 5°C is fit to Eq. (1.4b). The intercepts (stars on Y-axis) and slopes of the fits to Eq. (1.4a) are presented in Table 1.3.

Table 1.3: Fits to Eq. (1.4a) for 2D Dissolution

T (°C)	Homogenous Dissolution 0.01<|1/σ|<3.5		Defect-Assisted Dissolution 3.5<|1/σ|<25	
	Intercept $\ln\left(h\beta C_e(\omega^2 h n_s a)^{\frac{1}{3}}\right)$	Slope $\frac{\pi\alpha^2\omega h}{3(k_bT)^2}$	Intercept $\ln\left(h\beta C_e(\omega^2 h n_s a)^{\frac{1}{3}}\right)$	Slope $\frac{\pi\alpha^2\omega h}{3(k_bT)^2}$
5	-24.02 ± 0.02	-1.83 ± 0.04	N/A	N/A
12	-23.71 ± 0.04	-1.47 ± 0.03	-29.40 ± 0.90	-0.07 ± 0.11
21	-23.75 ± 0.01	-1.29 ± 0.03	-27.79 ± 0.25	-0.19 ± 0.04
37	-23.00 ± 0.11	-1.39 ± 0.06	-25.74 ± 0.26	-0.42 ± 0.05

By analyzing the fits to Eq. (1.4a) and making some simplifying assumptions, we can extract the physical parameters β, n_s, and α, and clarify their roles in setting the overall dissolution rate as a function of temperature. The intercepts and slopes are plotted in Figure **1.12** for homogenous ($0<\left|\frac{1}{\sigma}\right|<3.5$) and defect-assisted ($3.5<\left|\frac{1}{\sigma}\right|<10$) dissolution. The data are linear versus $1/T^2$ and are fit according to:

$$\text{Intercept}_{\text{2D}} = \ln\left(h\beta C_e(\omega^2 h n_s a)^{\frac{1}{3}}\right) = I_o + I_1 \cdot \frac{1}{T^2} \tag{1.5a}$$

$$\text{Slope}_{\text{2D}} = -\frac{\pi\alpha^2\omega h}{3(k_bT)^2} = S_o + S_1 \cdot \frac{1}{T^2} \tag{1.5b}$$

such that the overall rate is given by:

$$\text{Rate}_{\text{2D}} = \text{Intercept}_{\text{2D}} + \text{Slope}_{\text{2D}} \cdot \left|\frac{1}{\sigma}\right| = \left(I_o + I_1 \cdot \frac{1}{T^2}\right) + \left(S_o + S_1 \cdot \frac{1}{T^2}\right) \cdot \left|\frac{1}{\sigma}\right| \tag{1.5c}$$

I_1 and S_1 describe the temperature sensitivities of the intercept (proportional to β and n_s) and slope (proportional to α) terms of Eq. (1.4a). The values of I_o, I_1, S_o, and S_1 are listed in Table 1.4.

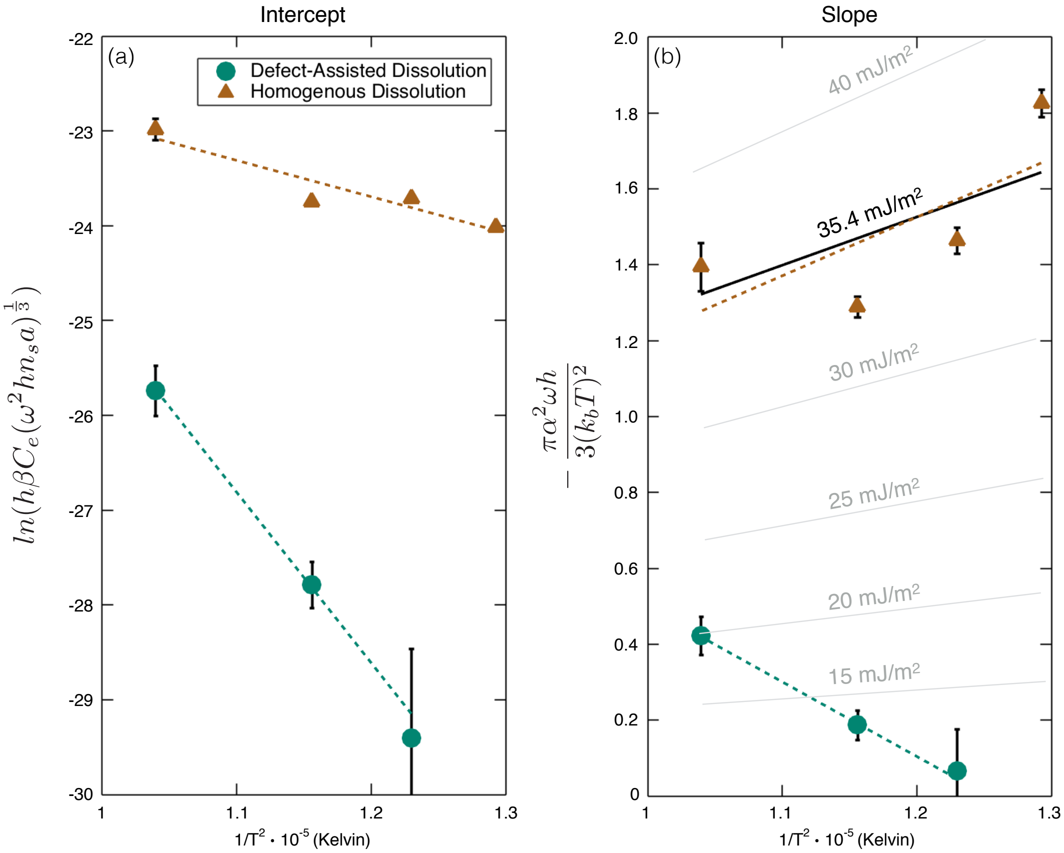

Figure 1.12: Temperature dependence of kinetic and energetic parameters of calcite dissolution in seawater. (a) Change in the intercept (proportional to β and n_s) and (b) slope (proportional to α) of the fit to Eq. (1.4a) for homogenous ($0<\left|\frac{1}{\sigma}\right|<3.5$, triangles) and defect-assisted ($3.5<\left|\frac{1}{\sigma}\right|<25$, circles) dissolution. Lines for constant α are plotted in (b) for comparison with the data. Fits to the data are presented in Table 1.4.

Table 1.4: Coefficients for the Observed Temperature Effect
on the Intercepts and Slopes of Equation (1.4a) for 2D Dissolution

	I_0	$I_1 \cdot 10^5$	S_0	$S_1 \cdot 10^5$
Homogenous 0.01<|1/σ|<3.5	-19.1 ± 1.18	-3.8 ± 1.0	0.33 ± 1.2	-1.5 ± 1.0
Defect-Assisted 3.5<|1/σ|<25	-5.82 ± 1.29	-19.1 ± 1.1	-2.38 ± 0.12	1.9 ± 0.1

1.4.2.1 Dissolution by Homogenous Etch Pit Formation

Homogenous dissolution exhibits a relatively weak temperature dependence in its β and n_s terms (Figure **1.12**a). We can isolate the effect of β on the intercept term by making the simplifying assumptions that β is independent of Ω and that n_s is saturated at its maximum value when calcite is undergoing homogenous 2D dissolution. Direct observations of homogenous 2D calcite dissolution in non-seawater solutions place the maximum n_s between 10^{12} (Teng, 2004) and 10^{13} sites/m^2 (Ruiz-Agudo et al., 2009). Assuming an average n_s of $5 \cdot 10^{12}$ sites/m^2, we solve for β using the fitted intercepts (Table 1.3), rearranging Eq. (1.5a), and substituting in the constants given in Table 1.5. The resulting βs are 0.40±0.02, 0.54±0.05, 0.53±0.01, and 1.17±0.26 cm/s at 5, 12, 21, and 37°C, respectively.

Table 1.5: Constants and calculated values for β, n_s and α

Variable	Units	Temperature (°C)				Source
		5	12	21	37	
m	-	1	1	1	1	-
h	m	$3\bullet10^{-10}$	$3\bullet10^{-10}$	$3\bullet10^{-10}$	$3\bullet10^{-10}$	1
a	m	$3\bullet10^{-10}$	$3\bullet10^{-10}$	$3\bullet10^{-10}$	$3\bullet10^{-10}$	1
w	m^3	$6.12\bullet10^{-29}$	$6.12\bullet10^{-29}$	$6.12\bullet10^{-29}$	$6.12\bullet10^{-29}$	2
P	m	$1.88\bullet10^{-9}$	$1.88\bullet10^{-9}$	$1.88\bullet10^{-9}$	$1.88\bullet10^{-9}$	3
K_{sp}	mol^2/kg^2	$4.309\bullet10^{-7}$	$4.318\bullet10^{-7}$	$4.296\bullet10^{-7}$	$4.151\bullet10^{-7}$	4
C_e	atoms/ m^3	$2.595\bullet10^{22}$	$2.600\bullet10^{22}$	$2.587\bullet10^{22}$	$2.500\bullet10^{22}$	5
Homogenous 2D Dissolution (Eq. 4a)						
$n_{s\_homogenous}$	sites/m^2	$5\bullet10^{12}$	$5\bullet10^{12}$	$5\bullet10^{12}$	$5\bullet10^{12}$	1, 6
β_{2D}	m/s	$4.0\pm0.02\bullet10^{-3}$	$5.4\pm0.05\bullet10^{-3}$	$5.3\pm0.01\bullet10^{-3}$	$11.7\pm0.26\bullet10^{-3}$	this study
$\alpha_{homogenous}$	mJ/m^2	-37.6±0.7	-34.5±0.8	-33.2±0.7	-36.5±1.6	this study
Defect-Assisted 2D Dissolution (Eq. 4a)						
n_{s_defect}	sites/m^2	-	$4.7\pm1.2\bullet10^{5}$	$2.5\pm0.1\bullet10^{7}$	$1.3\pm0.9\bullet10^{9}$	this study
α_{defect}	mJ/m^2	-	-6.8±5.9	-12.7±2.7	-20.1±2.3	this study
Step-Propagation (Eq. 4b)						
β_{step}	m/s	$3\bullet10^{-7}$	-	-	-	this study
α_{step}	mJ/m^2	-0.5	-	-	-	this study

[1] Teng (2004)

[2] From calcite density of 2.71g/cm^3

[3] Estimated assuming a burgers vector $b = mh$. $P = 2\pi b$, analogously to Dove et al. (2005)

[4] CO2SYS equilibrium K_{sp} in seawater at each temperature. Sal = 35 psu

[5] $K_{sp}/[Ca^{2+}]$, converted to molecules/m^3. $[Ca^{2+}]$=0.01M

[6] Ruiz-Agudo et al. (2009)

The βs we derive agree with those observed in AFM studies in non-seawater solutions. In the surface nucleation equations, the speed of a moving step, ν, is related to β and the solution saturation state via (Chernov, 1984; Malkin et al., 1989):

$$v = \omega\beta C_e(1 - \Omega) \tag{1.6}$$

By extrapolating to Ω=0 and substituting the values for w, C_e, and β at each temperature, we calculate upper limits for ν of 6.2, 7.8, 10.3, and 16.4 nm/s at 5, 12, 21, and 37°C, respectively. Although faster than typical calcite values of 0.5-4 nm/s (Arvidson et al., 2006;

De Giudici, 2002; Harstad and Stipp, 2007; Lea et al., 2001; Ruiz-Agudo et al., 2009), they are in the range for observations at the edges of coalescing etch pits of 7.9-14.3 nm/s (Vinson and Luttge, 2005). Etch pit coalescence is expected when the calcite surface is saturated with nucleation sites, so our high step speeds support our assumption that the mechanism in this Ω region is homogenous 2D etch pit formation. We note that these equivalences of β are based upon non-seawater measurements of n_s. If the saturated value of n_s is different in seawater, then our βs will change accordingly.

We can use the temperature dependence of our derived kinetic coefficients to estimate the activation energy of detachment from steps (ϵ_{step}) on the calcite surface. β is related to ϵ_{step} via an Arrhenius-style relation (Chernov, 1984; Malkin et al., 1989; Zhang and Nancollas, 1992; Xu et al., 2010, Eq. A.8 in appendix), and measuring the slope of ln(β) versus 1/T yields a value of -2700±700, corresponding with an ϵ_{step} of -22±6 kJ/mol (Figure 1.13a). This is the first estimate of ϵ_{step} for calcite dissolution in seawater. It agrees with the value of -25±6 kJ/mol derived from AFM measurements of β for obtuse step retreat (Xu et al., 2010), further lending confidence to the strength and sensitivity of our bulk solution measurement approach.

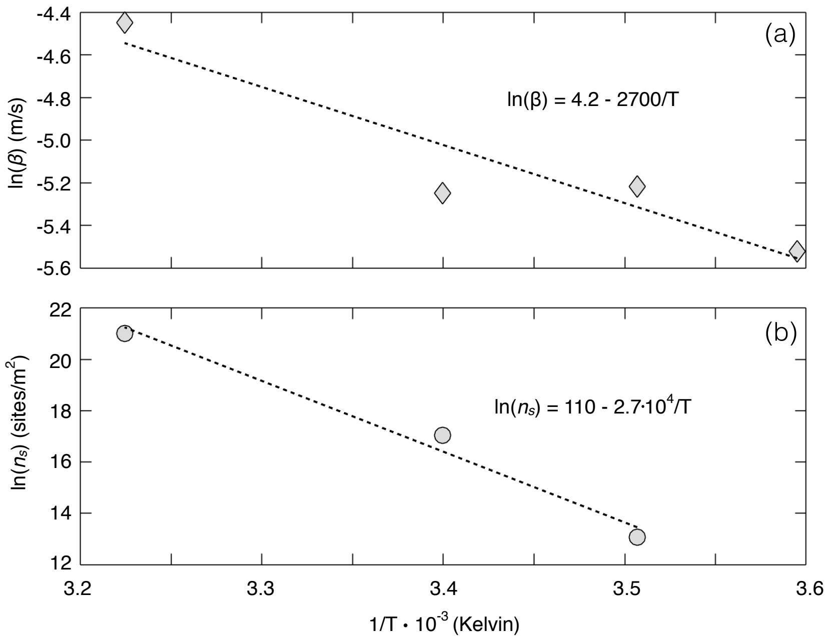

Figure 1.13: Arrhenius plots for the kinetic coefficient (a) and nucleation site density (b) derived from fits to Eq. (1.4a). (a) The slope of ln(*β*) versus 1/T is -2700±700, corresponding to an activation energy of detachment from kinks/steps of 22±6 kJ/mol. (b) The slope of ln(n_s) versus 1/T is 2.7±0.4•10^4, corresponding to a kinetic energy barrier to etch pit initiation of -230±30 kJ/mol.

Our calculated ϵ_{step} in seawater is not significantly different from that in freshwater, suggesting that changes in absolute ionic strength (IS) have little effect on step detachment energetics. Few studies have specifically measured the effect of IS on ϵ_{step}, so we cannot make a direct comparison with past research. The results are also unclear for the effects of IS on the bulk calcite dissolution/precipitation rate. Several studies have shown little to no effect of IS on calcite dissolution (Rickard and Sjöberg, 1983; Buhmann, 1987; Pokrovsky et al., 2005) and precipitation (Zhong and Mucci, 1989) rate, while others have found IS to catalyze precipitation (Zuddas and Mucci, 1998) and inhibit dissolution (Finneran and Morse, 2009; Gledhill and Morse, 2006). More remains to be done to understand how calcite dissolution mechanisms are affected by IS.

Our results further suggest that the sharp increase in rate at $\Omega \approx 0.75$, that has been reported in previous seawater studies (Berner and Morse, 1974; Dong et al., 2018; Keir, 1980; Subhas et al., 2015, 2017), occurs when calcite transitions from defect-assisted to homogenous 2D dissolution after overcoming a critical step edge free energy. β and n_s provide kinetic information on the dissolving calcite surface (i.e., how fast etch pits spread and how many sites are actively dissolving), but they do not tell us anything about the energetic constraints for when homogenous dissolution is activated. For this, we can look at the slopes of the data below $\left|\frac{1}{\sigma}\right|<3.5$, as they are proportional to α. The calculated slopes (Table 1.3) are plotted in Figure **1.12**b versus $1/T^2$ and overlaid with lines of constant α. The overlaid lines trend downward with increasing temperature because the slope term in Eq. (1.4a) also contains $1/T^2$. The trend for homogenous dissolution (Figure **1.12** triangles) follows a line of constant α = -35.4 mJ/m^2. Though the scatter appears large, the squared dependence on α means that the step edge free energies are well constrained. Averaging the α values in Table 1.5 across temperatures yields 35.4±2.0 mJ/m^2. This α is lower, but of the same order of magnitude as the 60-68 mJ/m^2 range calculated for the spontaneous precipitation of calcite in non-seawater solutions (Koutsoukos and Kontoyannis, 1984; Pokrovsky, 1998a). Our observation suggests that homogenous dissolution is activated on the calcite surface once a critical surface energy barrier, $\alpha_{\text{homogenous}}$ = -35.4±2.0 mJ/m^2, is surpassed, regardless of temperature. It may also explain our earlier observation in Section 1.1.1 for why bulk dissolution studies historically recover similar rates far from equilibrium in seawater. Each study had surpassed $\alpha_{\text{homogenous}}$ and was measuring the dissolution rate of a single mechanism, homogenous 2D etch pit formation.

1.4.2.2 Dissolution by defect-assisted etch pit formation

Temperature has a much larger effect in the region $3.5<\left|\frac{1}{\sigma}\right|<10$ associated with defect-assisted dissolution. According to Figure **1.12**a, the fitted intercepts for defect-assisted dissolution decrease with temperature by nearly four natural log units, compared to just one for homogenous dissolution. To understand this dependence, we must again attempt to distinguish between the effects of β and n_s on the intercept term of Eq. (1.4a). We can no longer assume a constant n_s, but our analysis of homogenous dissolution provides new constraints on the values and temperature dependencies of β. Both mechanisms initiate differently, but once started, they are assumed to proceed via the same opening and spreading of 2D pits. We therefore assume that the same βs that we calculated for homogenous dissolution also apply for defect-assisted dissolution. We refer to this shared term as β_{2D} and list its values in Table 1.5. Given this assumption, we solve for n_s by again rearranging the intercept term and substituting in the constants and β_{2D} from Table 1.5. We calculate active nucleation site densities of $4.7\pm1.2\cdot10^5$, $1.3\pm0.1\cdot10^7$, and $1.8\pm0.9\cdot10^9$ sites/m^2 at 12, 21, and 37°C, respectively. Increasing temperature increases the number of pit nucleation sites.

The temperature dependence of n_s is related to the kinetic energy barrier for removing an ion from the surface to initiate an etch pit, ϵ_{init}. (Eq. A.9 in appendix, Dove et al., 2005). This energy barrier is distinct from the step edge free energy, as ϵ_{init} is related to initiating an etch pit, whereas α is related to stabilizing an etch pit. Newly initiated pits will quickly be eliminated unless a critical free energy barrier, that is in turn dependent on α, T, and Ω per Eq. (A.6), is surpassed. Taking the natural log of n_s versus 1/T gives a value of $-2.7\pm0.4\cdot10^4$, corresponding with an ϵ_{init} of -230±30 kJ/mol (Figure 1.13b). This is the first time that ϵ_{init} has been estimated for calcite in seawater.

It is evident that the slope term for defect-assisted dissolution is strongly temperature dependent in a way that is not explained by the theory and runs counter to what was observed for homogenous dissolution. Whereas homogenous dissolution follows the prediction for a single, critical $\alpha_{homogenous}$, the energy barrier for defect-assisted dissolution, α_{defect}, changes by nearly a factor of three (S_1 terms in Table 1.4) and has the opposite temperature dependence. This suggests that opposing kinetic and energetic effects set the overall rate of defect-assisted dissolution. Temperature has a positive effect on calcite dissolution rate by increasing n_s and β, allowing for more active nucleation sites and faster pit spreading rates. Warmer temperatures also increase the local step edge free energy, though, making it more difficult to form a stable etch pit. The change in the temperature trend of α implies that there are additional factors beyond α, β, and n_s that influence near-equilibrium dissolution rates.

1.4.2.3 Dissolution by retreat of pre-existing steps

It is difficult to set experimental waters to Ωs very near equilibrium, but the limited number of points we have suggest that dissolution initiates via step retreat at all temperatures and continues from just under saturation until an Ω_{crit} near 0.9. Dissolution at 5°C skips the defect-assisted mechanism seen at warmer temperatures and maintains the curved slope indicative of step retreat (Eq. 1.4b) from saturation until $\Omega \approx 0.75$ (Figure **1.10**). Substituting in the constants in Table 1.5 to Eq. (1.4b), the 5°C data from $3.5 < \left|\frac{1}{\sigma}\right| < 25$ fit a step edge free energy of -0.5 mJ/m^2 and a β_{step} of $3 \cdot 10^{-5}$ cm/s. The kinetic coefficient required to fit the data is four orders of magnitude smaller than that used for homogenous/defect-assisted dissolution, but similar discrepancies between mechanisms have been seen in other minerals (Dove et al., 2005).

Of the temperatures investigated in this study, the 5°C experiments are most relevant to the modern ocean. The 5°C results are also the first evidence that the onset of a dissolution mechanism may be temperature dependent in seawater. We are unable to say with certainty why the defect-assisted dissolution mechanism is not activated, but one hypothesis is that the kinetic energy barrier to etch pit initiation is too large for etch pits to form at defects at 5°C. Projecting back the fitted intercept for defect-assisted dissolution reported in Table 1.4, we calculate an active nucleation site density of only 5 sites/cm^2 at 5°C. Considering that our grain size is on the 10s to 100s of microns scale, this would essentially mean that there are zero etch pits forming at defects. In this case, only step retreat is possible until the solution driving force overcomes $\alpha_{homogenous}$ and initiates homogenous dissolution.

Calcite has been shown to undergo simultaneous dissolution and precipitation across the full range of Ωs (Arakaki and Mucci, 1995; Subhas et al., 2017), so it is also possible that a temperature dependent change in the balance of these gross fluxes could explain the behavior we observe at 5°C. Precipitation is known to be influenced by the temperature and Mg:Ca ratio of the solution (Mucci, 1986; Mucci and Morse, 1984, 1983), and temperature dependent step changes in behavior have already been observed in the calcite system (Morse et al., 1997). Precipitation occurs preferentially at high-energy sites (Burton et al., 1951; Burton and Cabrera, 1949), so any change in its rate could suppress the formation of etch pits at defects. This effect would be amplified if there were few available defects. Since back-precipitation may be identified on our calcite grains by areas of elevated ^{12}C (Subhas et al., 2017), we will be able to quantify the role of back-precipitation in the future by dissolving calcite surfaces near equilibrium at low temperatures.

1.4.3 Role of Solution Chemistry

The surface theory has provided valuable insights into calcite dissolution mechanisms across a wide range of saturation states, but phenomena such as the reversal of the temperature dependence of α and the skipping of defect-assisted dissolution at 5°C indicate that the theory is not complete. The surface framework we have used contains only indirect information about the chemical speciation of the solution and the mineral surface itself, despite the known importance of these effects (Arakaki and Mucci, 1995; Pokrovsky et al., 2009; Sand et al., 2016 and references therein). The surface model encapsulates all the effects of speciation in its step edge free energy term. This is because α is dependent upon the local crystal bonding environment, and this bonding environment is affected by interactions with ions in solution (Chernov, 1984). The speciation of the calcite surface is well understood in dilute solutions (Oleg S. Pokrovsky et al., 2009; Pokrovsky, 1998b; Pokrovsky et al., 2005; Pokrovsky and Schott, 2002; Schott et al., 2009; Van Cappellen et al., 1993; Wolthers et al., 2008), and significant work has been done to relate these species to dissolution and precipitation kinetics (Arakaki and Mucci, 1995; Chou et al., 1989; Oleg S. Pokrovsky et al., 2009; Pokrovsky et al., 2005; Pokrovsky and Schott, 2002; Wolthers et al., 2012a). Surface speciation models have only recently begun to include interactions with individual major seawater ions such as SO_4^{2-} and Mg^{2+} (Song et al., 2017; Dobberschütz et al., 2018, and references therein), and these models have yet to be applied to the kinetics of seawater dissolution. Our measurements imply that a complete understanding of a dissolution rate law for calcite in seawater will require a surface energetic framework that incorporates the chemical complexation of the solution and mineral surface.

The role of solution chemistry on the dissolution rate of calcite in seawater has been supported by recent work by Subhas et al. (2017) using carbonic anhydrase (CA) to increase the re-equilibration rate of H_2CO_3 in seawater. With the addition of CA, the authors observed a ~250x increase in calcite dissolution rates above $\Omega>0.7$, compared to seawater at the same pH without CA. This saturation region is associated with defect-assisted dissolution, which is the mechanism we found to have the strongest temperature dependence. Given that the rate constant for the hydration of $CO_{2(aq)}$ to H_2CO_3 increases exponentially with temperature in dilute solutions (Wang et al., 2010), it is possible that the behavior we have observed for $\Omega>0.75$ may be partially explained by an elevation in the formation rate of H_2CO_3. Future work evaluating the temperature dependence of calcite dissolution in the presence of carbonic anhydrase will help to further parse the effects of solution chemistry and surface processes on the overall dissolution rate.

1.5 Conclusions

We dissolved ^{13}C-labeled calcite in seawater over a range of temperatures and found that the dissolution rate is highly non-linear across the full range of saturations. Although we recovered the same activation energy and dissolution rates at $\Omega = 0$ as those found in non-seawater solutions, the strong non-linearity of our data near equilibrium necessitated the use of a different mechanistic model beyond the traditional, empirical rate law, $R=k(1-\Omega)^n$. Using a surface-based framework developed by Dove et al. (2005), we found that our results were consistent with calcite dissolution being dominated by the retreat of pre-existing steps for $1>\Omega>0.9$, defect-assisted etch pit formation for $0.9>\Omega>0.75$, and homogenous etch pit formation for $\Omega<0.75$. Calcite surface energetics are dramatically altered by seawater, as the mechanistic transitions we identified occur significantly closer to equilibrium than they do in dilute solutions. The shift towards equilibrium suggests that ocean acidification may cause marine carbonates to enter faster dissolution regimes more readily than anticipated from previous studies. Our work also provides the first seawater estimates of kinetic coefficients (β), nucleation site densities (n_s), and step edge free energies for each mechanism (α), as well as the activation energy for detachment from steps (ϵ_{step}) and the kinetic energy barrier to etch pit initiation (ϵ_{init}). Several unexplained phenomena suggest that a complete theory will require the combination of a chemical speciation model with knowledge of the rate constants and energies we have measured for each of calcite's dissolution mechanisms.